

RSC Advances



This is an *Accepted Manuscript*, which has been through the Royal Society of Chemistry peer review process and has been accepted for publication.

Accepted Manuscripts are published online shortly after acceptance, before technical editing, formatting and proof reading. Using this free service, authors can make their results available to the community, in citable form, before we publish the edited article. This *Accepted Manuscript* will be replaced by the edited, formatted and paginated article as soon as this is available.

You can find more information about *Accepted Manuscripts* in the [Information for Authors](#).

Please note that technical editing may introduce minor changes to the text and/or graphics, which may alter content. The journal's standard [Terms & Conditions](#) and the [Ethical guidelines](#) still apply. In no event shall the Royal Society of Chemistry be held responsible for any errors or omissions in this *Accepted Manuscript* or any consequences arising from the use of any information it contains.

Recent advances in Mn-based oxides as anode materials for lithium ion batteries

Cite this: DOI: 10.1039/x0xx00000x

Yuanfu Deng,^{*a,b} Lina Wan,^a Ye Xie,^a Xusong Qin,^{*b} and Guohua Chen^{b,c}

Received 00th January 2012,
Accepted 00th January 2012

DOI: 10.1039/x0xx00000x

www.rsc.org/

It is of great interest to develop new electrode materials for lithium-ion batteries (LIBs), because the available electrode materials may not meet the high-energy demands for electronic devices, especially good cyclic and rate performance demands. Mn-based oxides have received substantial attentions as promising anode materials for LIBs due to their high theoretical specific capacities, low charge potential vs. Li/Li⁺, environmental benignity and natural abundance. Herein, the preparations of Mn-based oxide nanomaterials with various nanostructures and chemical compositions, and their application as negative electrodes for LIBs are reviewed. It covers MnO, Mn₃O₄, Mn₂O₃, MnO₂, CoMn₂O₄, ZnMn₂O₄ and their carbonaceous composites/oxides supports with different morphologies and compositions. The aim of this review is to provide an in-depth and rational understanding of the relationships among the chemical composition, morphologies and electrochemical properties of the Mn-based anode materials and how the electrochemical performance can be improved using materials engineering strategies. Special attention has been given to the discussion on some challenges and bottlenecks in the areas of practical applications of Mn-based oxides in LIB full cells.

1. Introduction

After entering the 21st century, the calling for more energy and a cleaner environment has forced a lot of countries to invest large amounts of money in developing the environmental friendly energy storage systems.¹ Rechargeable lithium-ion batteries (LIBs) have the advantages of high energy density, long cycle life and memory-free effect over the lead-acid battery, nickel–cadmium battery and nickel–metal hydride battery, making them widely applied in portable electronic and electric tool market.^{2–4} In the near future, they are expected to play even more important roles in electric vehicles (EVs) and plug-in hybrid electric vehicles (PHEVs).⁴ However, they currently still fail in meeting the demands dictated by powering of both EVs and HPEVs or by the large-scale energy storage systems for renewable energies. Therefore, a significant improvement in the lithium storage capacity is in imminent demand for LIBs to enhance their feasibility on the aforementioned large scale applications.

The charge/discharge mechanism of LIBs is based on the rocking-chair concept. A typical commercial LIB consists of a cathode (e.g., LiCoO₂) and an anode (e.g., graphite), together with an electrolyte-filled separator that allows lithium (Li) ions transfer but prevents electrodes from direct contact. When the battery is charging, Li ions deintercalate from the cathode and intercalate into the anode. Conversely, the Li ions intercalate into the cathode via the electrolyte during discharging. During

charge/discharge, Li ions flow between the anode and the cathode, enabling the conversion of chemical energy into electrical energy and the storage of electrochemical energy within the battery. The reactions in the typical battery are $\text{LiCoO}_2 + 6\text{C} \leftrightarrow \text{Li}_{1-x}\text{CoO}_2 + \text{Li}_x\text{C}_6$ ($0 < x < 1$).^{5–8}

The energy density of the LIBs depends on the capacities and operating potentials of the respective electrode materials. Searching for such electrode materials that can yield higher capacity and energy density, e.g. cathode materials with higher operating voltages (≥ 4.0 V vs Li/Li⁺)^{9–12} and anode materials with lower operating voltages (≤ 1.0 V vs Li/Li⁺), and are of less environmental cost is essential to achieve this goal.⁸ Research on anode materials for LIBs has been directed towards new materials that involves three different mechanisms: (1) intercalation–deintercalation mechanism, e.g. compounds with a two-dimensional (2-D) layer structure¹³ or three-dimensional (3-D) network structure¹⁴ that can reversibly intercalate/deintercalate Li⁺ into/out of the lattice; (2) elements (M) that can form alloys with Li metal (Li_xM), e.g. Si,^{15–17} Sn/SnO₂,^{18–23} Ge,²⁴ Sb,²⁵ Zn,²⁵ In, Bi, and Cd²⁷; and (3) materials that can act as anode with the so-called redox or “conversion” reaction with Li.²⁸ These materials are mainly oxides, fluorides, oxyfluorides, sulfides, nitrides and phosphides.²⁹ As the consequence, a large number and wide variety of metal-containing oxides, including binary and complex oxides have been explored for Li cycling.^{8,30–32} In

addition, the modern nanotechnology has been employed to prepare many metal oxides with various morphologies and structures for Li cycling as anode materials for LIBs.⁷ As a result, the research on metal oxides as anodes for LIBs has been enhanced and enriched very significantly in recent years.⁸

Among the metal oxides as anode materials for LIBs, Mn-based oxides have obvious advantages because of their high specific capacities, lower toxicity, cost, and operating voltage (average discharge and charge voltages of 0.5 V and 1.2 V vs. Li/Li⁺, respectively) comparing with the iron,³³⁻³⁵ cobalt³⁶⁻³⁸ and Ni-based oxides.³⁹⁻⁴⁰ Table 1 listed the experimental values of the plateaus potential and theoretical specific capacities associated with conversion reactions in Mn-based oxides.⁴¹⁻⁴⁵ In a Li/Mn_xO half-cell, the electrochemical processes can be summarized by the equation below:



This reaction for Li storage in Mn-based oxides based on the “conversion mechanism” has four major obstacles for practical applications:²⁹ (1) the strong structural reorganization that takes place to accommodate the chemical changes and induces large volume changes, resulting in severe particle agglomeration and unsatisfactory cycling performance; (2) low rate performance arising from their low conductivity; (3) an unacceptable large voltage hysteresis, in term of round-trip energy density loss, which is observed between the discharge and charge steps; and (4) a virtually ubiquitous large coulombic inefficiency observed in the first cycle.

[Table 1]

Different strategies have been proposed to resolve the aforementioned problems of Mn-based anodes, and four of them are widely practiced. The first strategy is to fabricate nanosized particles so as to shorten the diffusion length for electrons and lithium ions.⁴⁶ The second strategy is to synthesize Mn-based oxides with porous structure, which contains porous 1-D nanorods/nanowires⁴⁷ and hollow nanotubes,⁴⁸ 2-D nanoflakes,⁴⁹ and 3-D hollow or hierarchical porous nanostructures.⁵⁰ The vacant space provided by the hollow or porous structures can accommodate the structural strain and favor fast Li⁺ insertion/extraction kinetics by enabling electrolyte uptake through the nanoparticles, leading to improved rate and cycling performance. The third strategy is to introduce a considerable proportion of carbon into the Mn-based oxides to form homogenous oxides/carbon nanocomposites.⁴⁶ It has been suggested that the carbon-based materials can provide a cushion effect against the volume strain because of their elastic feature. Meanwhile, the carbon-based materials could also increase the electrical conductivity of the nanocomposites which is essential to the rate performance and cyclability. Furthermore, the carbon is also active at the low voltages at which some of the conversion reactions occur, thereby partially compensating the decrease in capacity associated with the dilution of the active phase. The fourth strategy is to optimize the electrodes by adjusting the ratios of active materials, binders and conductive agents or choosing novel binders/conductive agents.⁵¹ It has also been documented

that proper selection of the ratios of the active materials, conductive agents and binders would be an significant advantage for the improvement of the rate and cyclic performance for metal oxides-based⁵² and other anode materials.⁵¹ Because of the potential application of nano-scale Mn-based oxides as anode materials for LIBs, it is of great importance to have a more detailed discussion on this kind of metal oxides with various nanostructures, chemical compositions and their electrode fabrication processes.

Cabana *et al.*²⁹ gave an excellent review on the different conversion reactions of metal oxides, sulfides, nitrides, phosphides, and fluorides in 2010, in which the development of the Mn-based oxides as anode materials for LIBs before 2010 had been extensively reviewed. Wu *et al.*³⁰ gave a another good review on a topic of metal oxides as anode materials for LIBs in 2012. Reddy *et al.*⁸ reviewed the detailed development of metal oxides and oxysalts as anode materials for LIBs. Some advances in Mn-based oxides as anode materials for LIBs in recent years have also been found in these three papers. In addition, these three excellent review papers demonstrated that the research field of metal oxides as anode materials is a very active and important area of LIBs. Although some recent advances on this topic have been reviewed in aforementioned papers, continuous updating is still required to reflect the fast developments of the strategies for the electrochemical performance improvement of Mn-based oxides and their research statuses. In order to obtain better understanding of the research statuses of this topic, this review mainly discusses the recent developments, current status and the major strategies for the performance enhancement of Mn-based oxides with various structures and chemical compositions. The oxides reviewed in this work include MnO, Mn₃O₄, Mn₂O₃, MnO₂, CoMn₂O₄ and ZnMn₂O₄ as well their carbon/metal oxides-based composites. The key challenges and opportunities in their future developments and applications are also discussed. Given the rapid development and broad field of Mn-based oxides, the authors apologize for the inevitable oversights of some important contributions.

2. Binary Mn-based Oxides as anode materials

Mn-based binary oxides have been widely investigated as anode materials for LIBs in the past decades after the works of Tarascon *et al.* in 2000.²⁸ Many binary Mn-based oxides including MnO, Mn₃O₄, Mn₂O₃, MnO₂ and their carbon-based nanocomposites with different nano-structures have found useful applications in LIBs.⁸

2.1 MnO and its nanocomposites

Although the MnO has a high theoretical capacity of 755.6 mAh g⁻¹ that is twice the capacity of graphite, and a lower electromotive force (1.032 V vs Li/Li⁺) than other TMO anodes such as Fe₂O₃, Co₃O₄, NiO, CuO, and so forth, only few examples on the Li cyclability of the pure MnO anode material have been reported in recent years.^{46,49,53,54} This may attributed to the fact that manganese is one of the first row transition

metals which is very difficult to be reduced into a metallic state.²⁹ Zhong *et al.*⁴⁶ investigated the commercial MnO powders as anode active materials for LIBs. According to the results of *ex-situ* XRD, TEM and galvanostatic intermittent titration technique, they suggested that lithium is stored reversibly in MnO through conversion reaction and interfacial charging mechanism. In addition, they found that a layer of the solid electrolyte interphase with a thickness of 20–60 nm is covered on MnO particles after full insertion. The cyclic performance of MnO is significantly improved after decreasing particle size. Following this work, MnO in the forms of microspheres,⁵³ nanoflakes⁴⁹ and thin-film⁵⁴ as anode materials to improve their cycling and rate performance have been reported. In 2011, Zhong *et al.*⁵³ synthesized porous MnO microspheres by decomposing MnCO₃ under argon atmosphere at 600 °C for 1 h. The as-prepared MnO material shows a reversible capacity of 800 mAh g⁻¹ and an initial coulombic efficiency of 71%. It can deliver 600 mAh g⁻¹ at a rate of 400 mA g⁻¹. They further confirmed the conversion reaction mechanism by Mn K-edge X-ray absorption near edge structure (XANES) spectra and extended X-ray absorption fine structure (EXAFS), indicating that pristine MnO is reduced to Mn⁰ after discharging to 0 V and a part of reduced Mn⁰ is not oxidized to Mn²⁺ after charging to 3 V. Li *et al.*⁴⁹ developed a novel method for the preparation of porous MnO nanoflakes on nickel foam (Figs. 1a-d) by a reduction of hydrothermal synthesized MnO₂ precursor in hydrogen. The porous MnO nanoflakes showed good capacity retention capability and rate performance (Fig. 1e), with a capacity of 568.7 and 708.4 mA h g⁻¹ at the 2nd and 200th charge–discharge cycle at a current density of 246 mA g⁻¹ and 376.4 mA h g⁻¹ at a current density as high as 2460 mA g⁻¹, respectively. Thin films of MnO were successfully deposited on Cu foils by radio-frequency (RF) sputtering under the Ar:H₂ (95:5 vol%) reduction atmosphere at 500 °C.⁵⁴ The films with a thickness of about 0.5 μm exhibit an initial coulombic efficiency of 75% and a reversible specific capacity of 700 mAh g⁻¹ at 0.05 C after 100 cycles, and 428 mAh g⁻¹ at 20 C. These values demonstrate that the sputtering-grown MnO films exhibit excellent cyclability and rate performance in comparison to the MnO powders. They suggested that pure phase with low oxidation state and certain porosity could be favorable factors accounting for such improved electrochemical performance.

In addition to phase-pure MnO, the MnO-based nanocomposites have also been intensively studied as negative electrodes due to their improved electrochemical (Table 2).^{46, 55-74} The group of Li⁴⁶ synthesized carbon-coated commercial MnO (MnO-L) by ball milling with sugar followed by pyrolysis at 600 °C in Ar atmosphere (C/MnO-L) and found that a reversible capacity of ~650 mAh g⁻¹ at 50 mA g⁻¹ (0.08C) could be almost stable up to 150 cycles in the voltage range 0.01–3.0 V. Good rate performance with 400 mAh g⁻¹ at a rate of 400 mA g⁻¹ was also found. They have also demonstrated that the C/MnO-L nanocomposites have a lower voltage hysteresis (<0.7 V with a charging voltage of 1.2 V), during the discharge/charge cycles compared to other metal oxides.

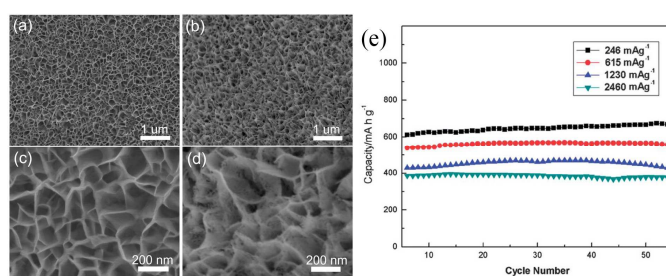


Fig. 1 (a), (b) Low-magnification SEM images of the samples before and after reduction; (c), (d) High-magnification SEM images of the samples before and after reduction; and (e) The discharge capacity at various current densities of MnO nanoflakes. Reproduced with permission.⁴⁹ Copyright 2012, RSC.

Inspired by the positive effect of carbon-coating, the MnO/C nanocomposites as anode materials for LIBs have received considerable interests.⁵⁵⁻⁵⁹ For example, unique amorphous MnO_x-C nanocomposite particles with interspersed carbon are synthesized using aerosol spray pyrolysis.⁵⁵ The amorphous MnO_x-C nanoparticles showed a high reversible capacity of approximately 650 mAh g⁻¹ under a current density of 200 mA g⁻¹, with exceptional capacity retention of 93% after 130 cycles. The coulombic efficiency of the amorphous MnO_x-C remained stable during the cycling after the first few cycles. They suggested that the 100% coulombic efficiency is attributed to the absence of new SEI formation during cycling, in which the carbon blocks liquid electrolyte penetration into MnO_x-C particles, reducing the contact area between MnO_x and electrolytes. Chae *et al.*⁵⁶ obtained a MnO_x/OMC (OMC = ordered mesoporous carbon) nanocomposite by a simple wet-impregnation of Mn(NO₃)₂ aqueous solution onto OMC nanorods followed by thermal treatment at 450 °C in an Ar flow (Fig. 2a). The MnO_x/OMC exhibited a high reversible capacity (>950 mAh g⁻¹) after 50 deep charge–discharge cycles with excellent cycling stability (Fig 2b), acceptable coulombic efficiency (97%) and good rate capability (750 mAh g⁻¹ at 1000 mA g⁻¹) (Figs. 2b-c). The incorporation of insulating and high density MnO_x into OMC nanorods exhibited synergistic benefits including higher volumetric as well as specific capacities, and smaller redox voltage hysteresis than OMC nanorods.

[Table 2]

Very recently, Luo *et al.*⁵⁷ have developed an efficient microwave-polyol process with a subsequent thermal treatment for the synthesis of MnO nanoparticles that are encapsulated uniformly in three-dimensional (3D) mesoporous interconnected carbon networks (MnO-MICN). Sodium citrate plays an important role on the morphology of the Mn-based precursors. An interesting phenomenon was observed for the nanocomposites as anode materials that the specific capacities (~30% of the overall capacity) gradually increase after 100 cycles. They suggested a new electrochemical reaction might occur. For instance, Mn²⁺ may be oxidized to a higher oxidation state. After 200 cycles at 200 mA g⁻¹, the specific discharge capacity reaches 1224 mA h g⁻¹ with a coulombic efficiency of ~99%. Moreover, a specific capacity of 731 mA h g⁻¹ is

retained after 200 cycles at 1500 mA g^{-1} , indicating good rate performance of the nanocomposites. Inspired by the natural microalgae with its special features (easy availability, biological activity, and carbon sources). Xia *et al.*⁵⁸ developed a green and facile biotemplating method to fabricate monodisperse MnO/C microspheres. Due to the unique hollow porous structure in which MnO nanoparticles were tightly embedded into a porous carbon matrix and form a penetrative shell, the MnO/C microspheres exhibited high reversible specific capacity of 700 mAh g^{-1} at 0.1 A g^{-1} , excellent cycling stability with 94% capacity retention after 50 cycles, and good rate performance of 230 mAh g^{-1} at 3 A g^{-1} . More recently, the nanocomposites of manganese monoxide and multi-walled carbon nanotubes (MnO/MWNTs) have been prepared hydrothermally by MWNTs and KMnO_4 followed with a sintering process.⁵⁹ The nanocomposites also show improved electrochemical performance as anode materials for LIBs, with a reversible capacity as high as $770.6 \text{ mA h g}^{-1}$ at the current density of 7.21 mA g^{-1} and good capacity retention (over 92.4% after 200 cycles at 216.14 mA g^{-1} between 0.01 and 3.0 V).

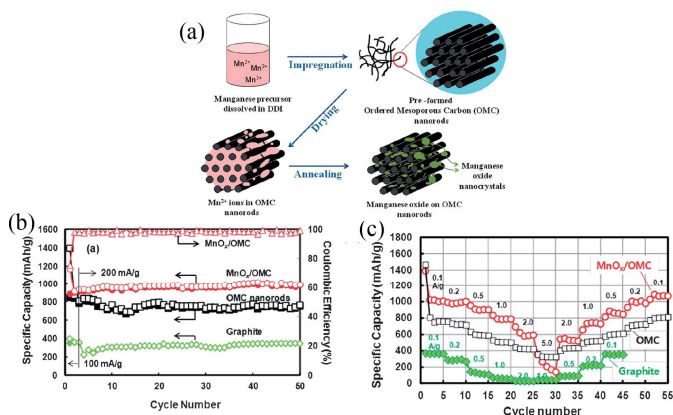


Fig. 2 (a) Schematic diagram for the preparation of MnO_x-loaded OMC nanorods; (b) Specific capacities OMC nanorods and MnO_x/OMC with cycle number; and (c) Rate performances of MnO_x/OMC, OMC nanorods and graphite cycled at different current densities. Reproduced with permission.⁵⁶ Copyright 2012, RSC.

It has been demonstrated that the strategy of preparing MnO/graphene composites is an effective route to obtain enhanced lithium-storage properties because graphene has superior conductivity, large surface area, structural flexibility, and chemical stability. In 2011, a composite of graphene nanosheets (GNs) supported by MnO nanocrystals was fabricated through a chemical-wet impregnation followed by the thermal reduction route.⁶⁰ The MnO-attached GN anode delivers a reversible capacity of 635 mAh g^{-1} at 0.2 C in the voltage range between 0.01 and 3.5 V, a high coulombic efficiency (92.7%) at the 1st cycle and good rate capability [capacity retention (5 /0.2 C: >70%)]. They also investigated the effect of Mn/C atomic ratio on the functions of the coulombic efficiency and found that the reversibility of Li⁺ intercalation/deintercalation gradually increases with the Mn atomic ratio. This result may be due to two major reasons: i) Mn ions tend to terminate dangling bonds located at the edges of

GNs, forming MnO-terminated edges of graphene fragments and (ii) appropriate amount of MnO spacers tend to stabilize the GN network, offering more active sites for reversible Li-storage. After this work, MnO/graphene nanocomposites with different MnO structures have been synthesized by different routes and used as anode materials for LIBs. Qiu *et al.*⁶¹ prepared a MnO nanoparticle/graphene composite (the diameters of the formed MnO nanoparticles are ranging from 20 to 250 nm) via *in-situ* carbothermal reduction of Mn₃O₄ on the surface of graphene nanosheets. The detachment and agglomeration of MnO nanoparticles were effectively prevented due to the tight combination of MnO nanoparticles and graphene. The MnO nanoparticle/graphene composites show a high specific capacity of approximately 700 mAh g^{-1} at 100 mA g^{-1} , excellent cyclic stability, and good rate capability as anode material for LIBs. Zhang *et al.*⁶² synthesized nitrogen-doped MnO/graphene nanosheets (N-MnO/GNS) hybrid material by a hydrothermal method followed by ammonia annealing (Fig. 3a). Because of its unique N-doped nanostructure and efficiently mixed conducting network, this nanostructured hybrid exhibited a reversible electrochemical lithium storage capacity as high as 772 mAh g^{-1} at 100 mA g^{-1} after 90 cycles (Fig. 3b), and an excellent rate capability of 202 mA h g^{-1} at a high current density of 5 A g^{-1} (Fig. 3c).

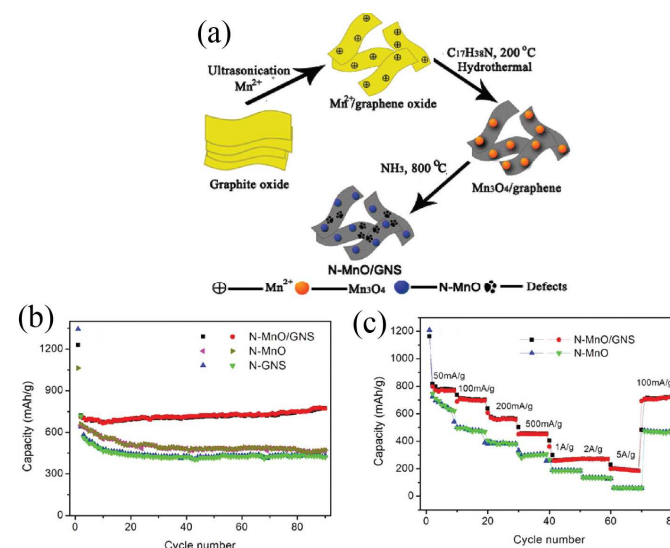


Fig. 3 (a) Schematic illustration for the preparation of N-MnO/GNS hybrid material; (b) Comparison of cycling performance of N-MnO, N-GNS, and N-MnO/GNS hybrid at a current density of 100 mA g^{-1} ; and (c) Rate capability of N-MnO and N-MnO/GNS at various current densities. Reproduced with permission.⁶² Copyright 2012, ACS.

Mai *et al.*⁶³ synthesized a MnO/reduced graphene oxide sheet (MnO/RGOS) hybrid by a two-step electrode design consisting of liquid phase deposition of MnCO₃ nanoparticles on the surface of graphene oxide sheets followed by heat treatment in nitrogen flow. The MnO/RGOS hybrid electrode shows a reversible capacity of $665.5 \text{ mA h g}^{-1}$ after 50 cycles at a current density of 100 mA g^{-1} and delivers $454.2 \text{ mA h g}^{-1}$ at a rate of 400 mA g^{-1} . It is found that the MnO/RGOS hybrid electrode exhibits an enhanced reversible capacity with respect

to that of MnO electrode, which is attributed to the re-oxidation from the Mn/Li₂O nanocomposite to MnO nanoparticles. In addition, they suggested that the incorporation of RGOS is not very effective for the decrease of the hysteresis voltage of MnO electrode by galvanostatic intermittent titration technique (GITT) as well as electrochemical impedance spectroscopy (EIS). This remarkable hysteresis has both thermodynamic and kinetic origins. In 2013, Sun *et al.*⁶⁴ reported a facile solution-based method combined with a subsequent reduction process for the large-scale fabrication of a MnO/graphene nanocomposite. The prepared MnO/graphene hybrid anode exhibits an initial reversible capacity of around 890.7 mAh g⁻¹ at a current density of 200 mA g⁻¹ and a reversible capacity as high as 2014.1 mAh g⁻¹ after 150 discharge/charge cycles (Fig. 4). In addition, the composite shows excellent rate capability (625.8 mAh g⁻¹ at 3000 mA g⁻¹) and superior cyclability (843.3 mAh g⁻¹ even after 400 cycles at 2000 mA g⁻¹ with only 0.01% capacity loss per cycle). The specific capacity is much higher than the theoretical capacities of both MnO (~ 756 mAh g⁻¹) and graphene (~ 744 mAh g⁻¹). The lithiation and delithiation behaviors suggest that the further oxidation of Mn(II) to Mn(IV) which is similar to the recent report of Luo *et al.*,⁵⁷ and the interfacial lithium storage upon cycling have significant contributions to the specific capacity enhancement.

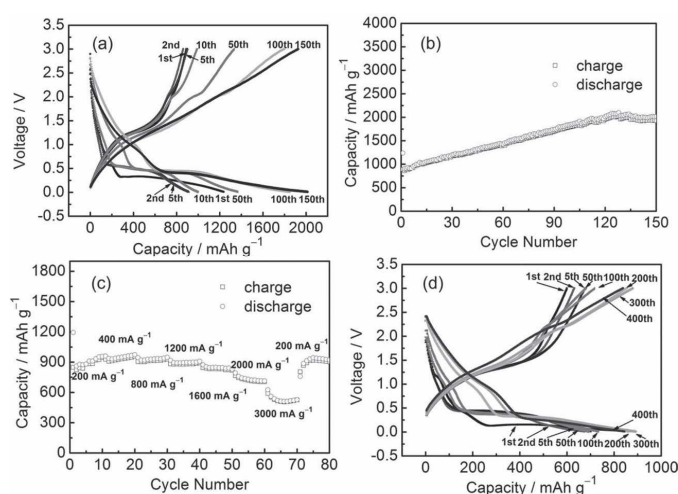


Fig. 4 (a) Discharge and charge voltage profiles of the obtained MnO/graphene product at a current density of 200 mA g⁻¹; (b) Cycling performance of the prepared MnO/graphene hybrid electrode cycled at 200 mA g⁻¹ and (c) at various current densities of 200, 400, 800, 1200, 1600, 2000, and 3000 mA g⁻¹; and (d) Discharge and charge curves at a current density of 2000 mA g⁻¹. All carried out in the voltage range 3–0.01 V vs. Li. Reproduced with permission.⁶⁴ Copyright 2013, Wiley.

One dimensional (1-D) nanostructures have attracted considerable attention as anode materials for LIBs, since they allow better accommodation of volume changes during repetitive charge/discharge cycles and the 1-D nanostructure possesses direct one-dimensional electronic pathways for efficient charge transport. In 2011, the 1-D coaxial MnO/C nanotubes with an average diameter of about 450 nm, a wall thickness of about 150 nm, a length of 1–5 μm and a 10 nm thick carbon layer were first reported by Ding *et al.*,⁶⁵ using β-

MnO₂ nanotubes as self-templates in acetylene at 600 °C. This sample exhibits a reversible capacity of about 500 mAhg⁻¹ at a current density of 188.9 mA g⁻¹, and 83.9% of capacity retention. Although the as-prepared sample shows better lithium storage properties compared to the bare MnO nanotubes (58.2%) and MnO nanoparticles (25.8%), its electrochemical performance is still not satisfactory due to the quick capacity fading. The enhanced reversible capacity and cycling stability for coaxial MnO/C-NTs are attributed to the conductive carbon layer on the MnO nanotubes, which can provide improved electronic transport to MnO nanotube core and be considered as a buffering layer to alleviate the volume changes caused by repetitive cycling. In recent years, the reduction of MnO_x (x > 1) with special nanostructure features has been appeared to be more widely practiced. Wang's group⁶⁶ synthesized MnO/C core-shell nanorods by an *in-situ* reduction method using MnO₂ nanowires as precursor and block copolymer F127 as carbon source in a gas flow of 5 vol.% H₂ in Ar. The as-prepared MnO/C core-shell nanorods exhibit a higher specific capacity than MnO microparticles as anode material for lithium ion batteries, with a specific discharge capacity of about 700 mAh g⁻¹ after 40 cycles under a current density of 200 mA g⁻¹. Li *et al.*⁶⁷ reported a facile synthetic method for the preparation of MnO@carbon core-shell nanowires with a jointed appearance, based on the reduction of Mn₂O₃ precursors followed by graphitization of C₂H₂. The MnO@carbon core-shell nanostructures could deliver reversible capacities as high as 801 mAh g⁻¹ at a high current density of 500 mA g⁻¹, with excellent electrochemical stability over 200 cycles. The remarkable electrochemical performance is mainly attributed to the highly uniform carbon layer around the MnO nanowires, which is not only effective in buffering the structural strain and volume variations of anodes during repeated electrochemical reactions, but also greatly enhances the conductivity of the electrode material. They also suggested that their strategy is simple but very effective, and appears to be sufficiently versatile and extended to other high-capacity electrode materials with large volume variations and low electrical conductivities. More recently, Zhu's group⁶⁸ has developed a novel route to synthesize MnO@1-D carbon composites through a pyrolysis process, using C₄H₄MnO₆ as the single molecule precursor. The MnO nanoparticles are uniformly dispersed inside or adhered to the surface of the 1-D carbon nanotubes, and these carbon nanotubes overlap each other to form carbon scaffolds. This special structure feature not only improves the electronic conductivity, but also provides a support for loading MnO nanoparticles, resulting in a high specific capacity (1482 mA h g⁻¹ at 200 mA g⁻¹), good rate performance (420 mA h g⁻¹ at 2.0 A g⁻¹) and excellent capacity retention capability (810 mA h g⁻¹ at 1460 mA g⁻¹ after 1000 cycles).

The solvo/hydrothermal approach has been proved to be a suitable route for the preparation of 1-D MnO/C nanocomposites. For examples, Sun's group⁴⁸ developed a facile hydrothermal method followed by thermal annealing to synthesize porous MnO/C nanotubes (Fig. 5). Electrochemical results demonstrate that the porous MnO/C nanotubes could

deliver a reversible capacity as high as 763.3 mAh g⁻¹ after 100 cycles at a charge/discharge current density of 100 mA g⁻¹ (0.13 C, 1 C = 755.6 mA g⁻¹), and 618.3 mAh g⁻¹ after 200 cycles at a rate of 0.66 C (Fig. 6). They suggested that the superior cyclability and rate capability are attributed to the hollow interior, porous structure, 1D structure and the uniformly dispersed carbon in the porous MnO/C nanotubes. Su *et al.*⁶⁹ reported a two-step hydrothermal treatment and subsequent sintering at 600 °C to prepare hierarchical MnO@C nanorods using KMnO₄ and citric acid as raw materials. The ultra-small MnO nanocrystals (< 5 nm) were homogeneously dispersed in a carbon matrix and further coated with a well-proportioned carbon shell. This sample exhibited a reversible capacity of 481 mA h g⁻¹ after 50 cycles at a current density of 200 mA g⁻¹, which is higher than that of carbon-coated MnO nanoparticles.

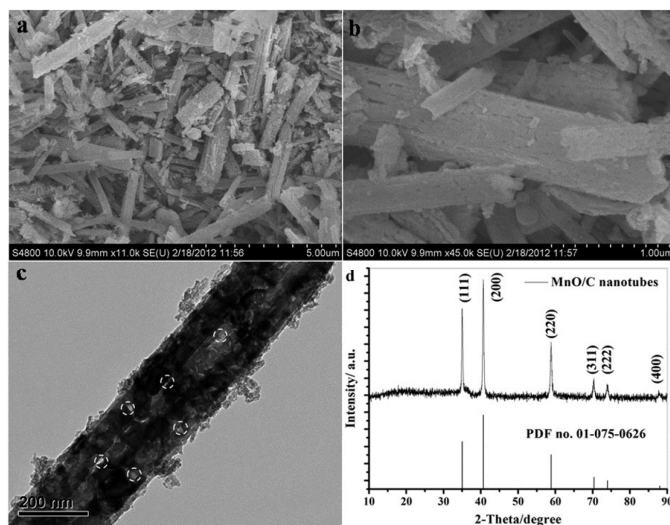


Fig. 5 (a) Low and (b) high magnification SEM images; (c) TEM image and (d) XRD pattern of the porous MnO/C nanotubes. Reproduced with permission.⁴⁸ Copyright 2012, RSC.

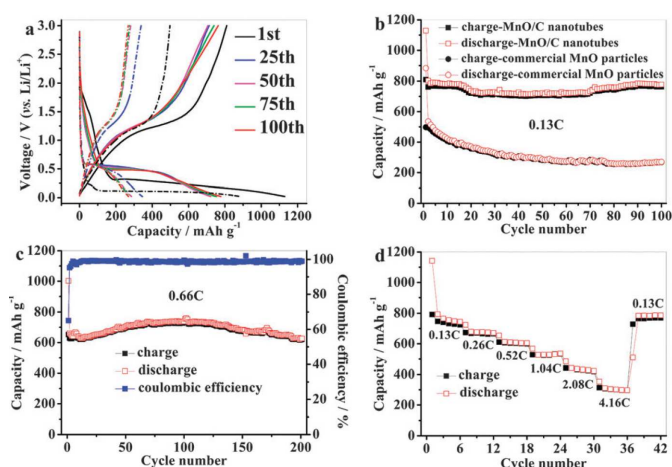


Fig. 6 (a) Charge/discharge curves and (b) cycle performances of commercial MnO particles (short dash dot) and the porous MnO/C nanotubes (solid) at a charge/discharge rate of 0.13 C; (c) cycle performance of the porous MnO/C nanotubes at a charge/discharge rate of 0.66 C; (d) rate performance of the porous MnO/C nanotubes. Reproduced with permission.⁴⁸ Copyright 2012, RSC.

The 2-D nanostructures of MnO-based nanocomposites are not as well researched as their 1-D counterparts. The reason probably lies in the difficulty in fabricating well-defined MnO-based nanocomposites. Sun *et al.*⁷⁰ prepared porous carbon-modified MnO disks with about 50 nm in average thickness and up to 3 mm in diameter by a microwave-polyol process followed by thermal annealing of the disk-like Mn-complex precursor. In their work, they demonstrated that each C–MnO disk has a single-crystal-like nature and is built up by the assembly of carbon-modified MnO nanocrystals of ~12 nm through the same crystallographic orientation. Because the unique assembled nano-architecture involving three-dimensionally interconnected nanopores and carbon modification as well as small particle sizes of MnO nanocrystals, the as-synthesized C–MnO nanocomposites exhibit high capacity (an initial capacity of 1387.2 mA h g⁻¹ with a coulombic efficiency of 71.9% at a current density of 100 mA g⁻¹ in the first cycle) and excellent cycling stability (a reversible capacity of 1044.2 mA h g⁻¹ after 140 cycles at 100 mA g⁻¹). It is also worthy to note that the capacity first drops then increases upon cycling, which has been observed in the case of MnO/C,⁵³ MnO/reduced graphene oxide⁶³ and MnO_x/C.⁵⁵ They suggested that the mechanism behind the U-shaped curve of capacity retention is not clear, but may be attributed to the formation of high oxidation state products⁴⁹ or mixed effects of Mn cluster aggregation and reversibility improvement of the conversion reaction in manganese oxide due to the formation of defects and deformation.⁵⁵ Although the carbon materials (amorphous carbon, carbon nanotube and graphene) have apparent beneficial effects on the electrochemical cycling and rate performance of the MnO-based composites, they have very low electrochemical activity and limited lithium storage capacity. Therefore, the carbon content in the composites needs to be carefully adjusted in order to find a balance between the capacity and the cycle life of the electrode. Chen's group⁶¹ synthesized carbon-coated nano-MnO powders (MnO/C) with different carbon contents by reduction of Mn₃O₄ with a particle size of about 20 nm, using glucose as both carbon source and reducing agent. The electrode fabricated using 10.7wt% carbon-coated MnO/C shows the best cycling stability and rate performance, with a high reversible capacity of 939.3 mAh g⁻¹ after 30 cycles at 0.1 C. By controlling the treatment temperature and reaction time, Zhang *et al.*⁷² synthesized MnO@C core-shell nanoplates with controllable carbon shell thickness via thermal treatment deposition of acetylene on the Mn(OH)₂ nanoplates precursor (Fig. 7a). When controlling the temperature of carbon-decoration and the reaction duration time, the thickness of the carbon shell can be tuned from 3.1 to 13.7 nm. The electrochemical experimental results show that the MnO@C nanoplates with a carbon shell thickness of 8.1 nm display a higher reversible capacity (770 mAh g⁻¹ at a current density of 200 mA g⁻¹) and better cyclability than those of nanoplates with carbon shell thicknesses of 3.1, 4.0, 4.2, 10.9 and 13.7 nm (Fig. 7b).

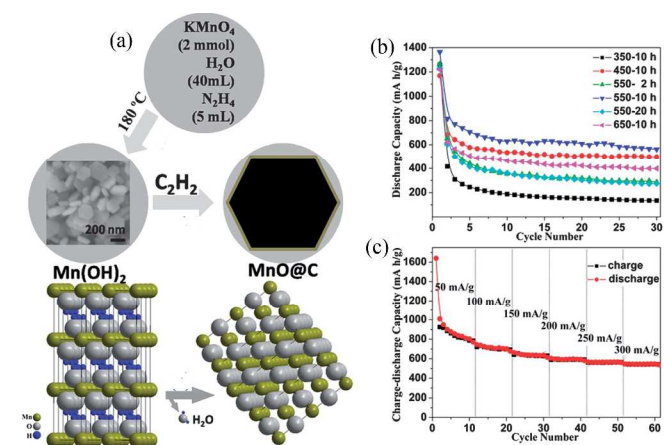


Fig. 7 (a) Schematic illustrating the formation process of the MnO@C; (b) Discharge capacity vs. cycle number for MnO@C products synthesized at different conditions at a current density of 200 mA g⁻¹; and (c) The rate performance of the MnO@C products synthesized at 550 °C for 10 h. Reproduced with permission.⁷² Copyright 2012, RSC.

In summary, results from this series of studies show that, despite the high theoretical capacities of MnO and the improved cyclic and rate performance by many strategies, however, these data were obtained through the Li/MnO half-cells. Up to now, few papers^{73,74} have reported the full cells using MnO-based oxides as anode and LiMn₂O₄, and LiNi_{0.5}Mn_{1.5}O₄ as cathode. A lithium ion battery using LiMn₂O₄ as cathode and MnO_x/mesoporous carbon as anode has been reported by Lee *et al.*⁷³ The capacity of the MnO_x/C anode decayed gradually from 700 mAh g⁻¹ to 500 mAh g⁻¹ after 100 cycles, and the MnO_x/mesoporous carbon/LiMn₂O₄ full cell operates at an average working voltage of 3.3 V with a capacity of 105 mAh g⁻¹ (Fig. 8).

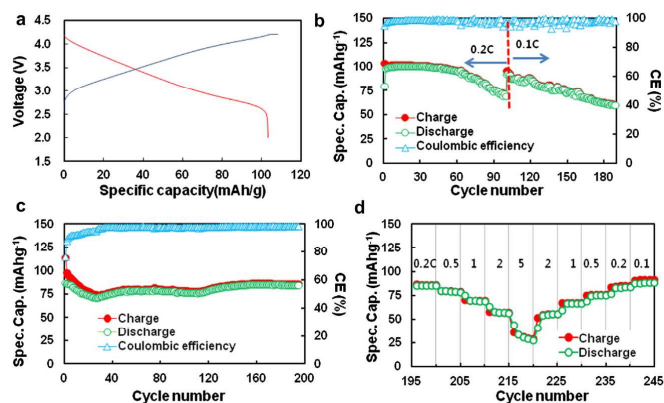


Fig. 8 (a) Voltage profile; (b) Cycling performance of LMO-MnO_x/C (A) cell at 0.2 C for 100 cycles and then at 0.1 C for up to 188 cycles; (c) Cycling performance of LMO-MnO_x/C (B) cell at 0.2 C for up to 195 cycle; and (d) Rate performance of LMO-MnO_x/C (B) cell. Voltage cut-off range is between 2.0 and 4.1 V. Reproduced with permission.⁷³ Copyright 2013, Elsevier.

In a recent paper, Sun's group⁷⁴ successfully developed a facile route to synthesize hierarchical micro/nanostructured MnO anode and spinel LiNi_{0.5}Mn_{1.5}O_{4-δ} cathode materials by using hierarchical micro/nanostructured MnCO₃ with olive shape as precursor. Both the MnO and LiNi_{0.5}Mn_{1.5}O_{4-δ} materials

possess excellent lithium storage properties owing to their unique hierarchical micro/nanostructures. The MnO in a MnO/Li half-cell can deliver a reversible capacity of 782.8 mAh g⁻¹ after 200 cycles at a rate of 0.13 C, and a stable reversible capacity of 350 mAh g⁻¹ at a high rate of 2.08 C. A full lithium ion battery using the MnO as anode and the LiNi_{0.5}Mn_{1.5}O_{4-δ} as cathode demonstrates a high discharge specific energy ca. 350 Wh kg⁻¹ after 30 cycles at 0.1 C with an average working voltage at 3.5 V and a long cycle stability. The MnO/LiNi_{0.5}Mn_{1.5}O_{4-δ} full cell can maintain a discharge specific energy of 227 Wh kg⁻¹ after 300 cycles at a higher rate of 0.5 C (Fig. 9). Considering these two successful examples, the full cells assembled by MnO-based nanocomposites anode may present a promising potential application for next generation of LIBs.

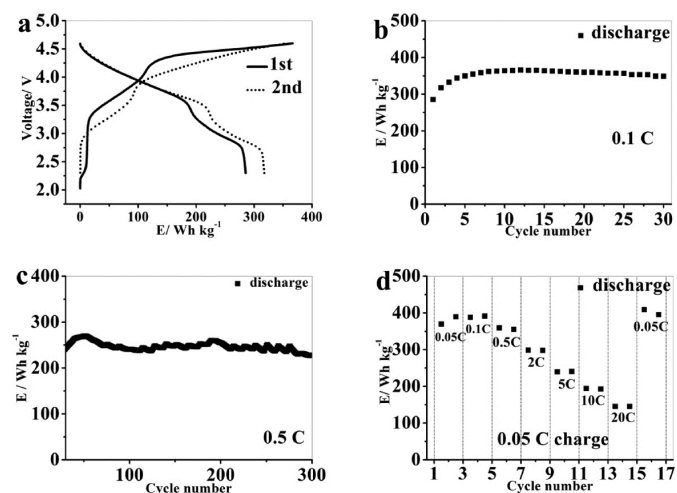


Fig. 9 (a) Charge/discharge profiles and (b) cycling performance of the MnO/LNMO full cell at a rate of 0.1 C; (c) cycling performance of the MnO/LNMO full cell at a rate of 0.5 C; and (d) the discharge specific energies of MnO/LNMO full cell at different rates (0.05 C charge). Reproduced with permission.⁷⁴ Copyright 2013, ACS.

2.2 Mn₃O₄ and its nanocomposites

In 1983, the group of Goodenough⁷⁵ reported the electrochemical insertion of Li into Mn₃O₄. However, few literatures⁷⁵⁻⁷⁸ have reported on this material as anode material for LIBs partially due to its extremely low electrical conductivity (~10⁻⁷-10⁻⁸ S cm⁻¹), limiting its capacity to ~400 mAh g⁻¹ even with Co doping. The optimization of synthesis conditions is therefore necessary to obtain single-phase Mn₃O₄ material. In 2010, Li's group⁷⁹ reported a facile solvothermal process for the controllable synthesis of the Mn₃O₄ nanocrystals with different sizes and shapes, which includes dots, rods, and wires with the presence of the surfactants of dodecanol and oleylamine. The as-prepared monodisperse nanocrystals, acting as ideal building blocks, can be rationally assembled into three-dimensional (3D) Mn₃O₄ colloidal spheres, using a facile ultrasonication strategy. This paper gave a good example for the preparation of pure Mn₃O₄ nanomaterials. After that, this mixed-valent oxide (Mn₃O₄) and its nanocomposites have been

extensively investigated as anode material by “conversion reaction” of lithium and continue to be studied (Table 3).⁸⁰⁻⁸⁹ Shen *et al.*⁸⁰ synthesized Mn_3O_4 nanorods with diameters of 50–150 nm and lengths of about 1–2 μm via the heat-treatment of the MnCO_3 nanorods, which were obtained from a facile hydrothermal method, in nitrogen atmosphere. When applied as anode materials for lithium ion batteries, the Mn_3O_4 nanorods exhibited a reversible lithium storage capacity of 1050 mAh g^{-1} in the first a few cycles. However, the pure Mn_3O_4 nanorods show a rapid capacity loss with the increase of the cycle number and the capacity decreased to 108 mAh g^{-1} at the 100th cycle. Engineering the morphology of Mn_3O_4 nanomaterials has been an effective strategy to enhance their electrochemical performance. Therefore, other pure Mn_3O_4 with different morphologies and microstructures, including octahedral Mn_3O_4 crystals with exposed high-energy facets⁸¹, spongelike Mn_3O_4 nanostructures,⁴³ mesoporous stacked Mn_3O_4 nanosheets,⁸² foamlike porous Mn_3O_4 ,⁸³ mesoporous Mn_3O_4 nanotubes,⁸⁴ order-aligned Mn_3O_4 nanostructures⁸⁵ and Mn_3O_4 octahedrons with a typical diameter around 300–400 nm,⁸⁶ have been synthesized and intensively investigated as anode materials for LIBs. In these Mn_3O_4 nanomaterials, the mesoporous Mn_3O_4 nanotubes⁸⁴ and Mn_3O_4 octahedra⁸⁶ show high specific capacities and excellent cycling performance. Specifically, the mesoporous Mn_3O_4 nanotubes⁸⁴ with a high surface area of 42.18 $\text{m}^2 \text{g}^{-1}$ and an average pore size of 3.72 nm, obtain from the hydrogen reduction of $\beta\text{-MnO}_2$ nanotubes under a H_2/Ar atmosphere at 280 $^\circ\text{C}$ for 3 h, exhibit a high specific capacity of 641 mA h g^{-1} after 100 cycles at a high current density of 500 mA g^{-1} (Fig. 10). The Mn_3O_4 octahedra,⁸⁶ which was straightforwardly prepared at room temperature using a one-step dealloying method (Fig. 11a), have an ultra- long cycle life with capacity retentions of 81.3% and 77.8% after 500 cycles at 100 and 300 mA g^{-1} , respectively (Fig. 11b and 11c).

[Table 3]

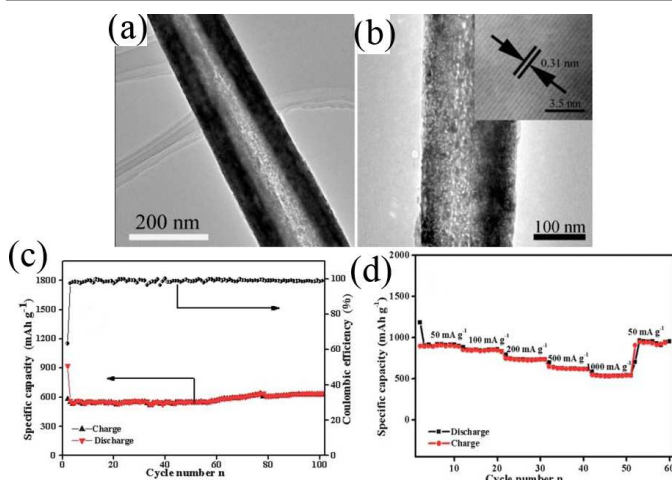


Fig. 10 (a) TEM and (b) HRTEM images of mesoporous Mn_3O_4 nanotubes; (c) Cycle performance and coulombic efficiency versus cycle number of Mn_3O_4 nanotubes at a current density of 500 mA g^{-1} and (d) Rate capabilities with increasing current density. Reproduced with permission.⁸⁴ Copyright 2013, RSC.

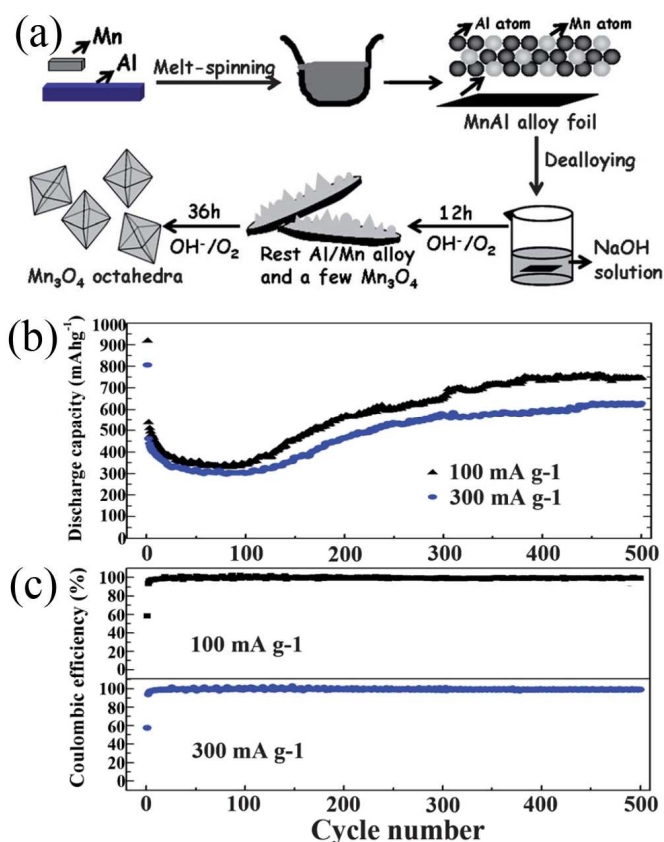


Fig. 11 (a) The schematic fabrication of the Mn_3O_4 octahedra; (b) Cycling behavior; and (c) Coulombic efficiency of the Mn_3O_4 anode at different current densities. Reproduced with permission.⁸⁶ Copyright 2014, RSC.

In order to tackle the problem of low capacity retention capability of the pure Mn_3O_4 material, researchers have designed M-doped Mn_3O_4 ($M = \text{Co}, \text{Fe}$ and Cu) samples.^{76,87-89} In 2005, Shen *et al.*⁷⁶ synthesized Co-doped Mn_3O_4 sample to improve the cycling performance of pure Mn_3O_4 phase. The Co-doped Mn_3O_4 sample delivers a specific capacity of 400 mA h g^{-1} , which is much higher than the specific capacity of pure Mn_3O_4 ($\sim 200 \text{ mA h g}^{-1}$). More recently, Ma *et al.*⁸⁷ prepared Fe-doped Mn_xO_y with connected macropores and mesopores to provide a hierarchical porosity by a facile and scalable nanocasting technique followed by controlled calcination, using a novel macroporous amine-functionalized bromomethylated poly (2,6-dimethyl-1,4-phenylene oxide) (BPPO) membrane as the sacrificial template (Fig. 12). The macropores in the final product were mainly formed by the reversible replication of the membrane porous structure, and interconnected branches in the pore system. The macropores cushioned the volume change in the conversion reaction of lithium during cycling, and also acted as reservoirs and thoroughfares to improve Li^+ transport in the electrolyte phase. The mesopores between primary nanocrystalline particles were formed upon heat treatment, and provided the large interfacial contact between electrolyte and electrode active material to support a high Li^+ flux across the solid/liquid interface. The selection of iron as a dopant was intentional: the redox potential

of iron (1.0 V for discharge/1.7 V for charge) is higher than that of manganese (0.5 V for discharge/1.2 V for charge)⁹⁰. Therefore, the evenly distributed iron could remain in the zero valent state during a large part of Mn_xO_y conversion reaction, serving conceptually the dual function of (1) electrical wiring of the electro-active material to lower the resistance for electron transport and (2) promoting ionic conduction by creating narrowly spaced interfaces at the oxide grain boundary. As anticipated, the Fe-doped Mn_xO_y composites show good capacity retention and high rate capabilities, delivering a capacity of $\sim 400 \text{ mAh g}^{-1}$ at 1500 mA g^{-1} after 900 cycles (Fig. 13). In the work, they synthesized manganese oxides doped with different amounts of iron and investigated the effect of Fe content on the phase structures and electrochemical performance of the as-synthesized samples. These results indicate the importance of a moderate level of iron doping to balance its effects on interfacial charge transfer and the structural integrity of the mesopores. Further studies are required to explore the effect of metal dopants on the rate and long-term cycling performance as well as the columbic efficiency of Mn_3O_4 composites.

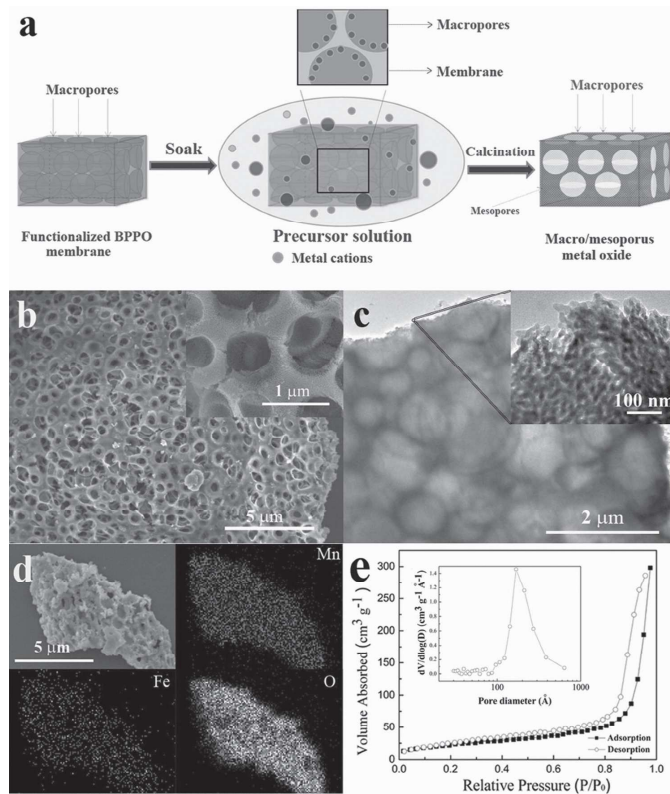


Fig. 12 (a) Schematic illustration of the preparation of hierarchical macro/mesoporous metal oxide structures; (b) FESEM images at low and high magnifications (inset of Fe-doped Mn_3O_4 -2); (c) TEM images at low and high magnifications (inset of Fe-doped Mn_3O_4 -2); (d) SEM image of Fe-doped Mn_3O_4 -2 and EDX element maps of Mn, Fe, and O; and (e) Nitrogen adsorption-desorption isotherms of Fe-doped Mn_3O_4 -2 and corresponding pore size distribution (inset). Reproduced with permission.⁸⁷ Copyright 2013, Wiley.

Mn_3O_4 -graphene hybrid as a high capacity anode material for LIBs was first investigated by Cui's group.⁹¹ They developed

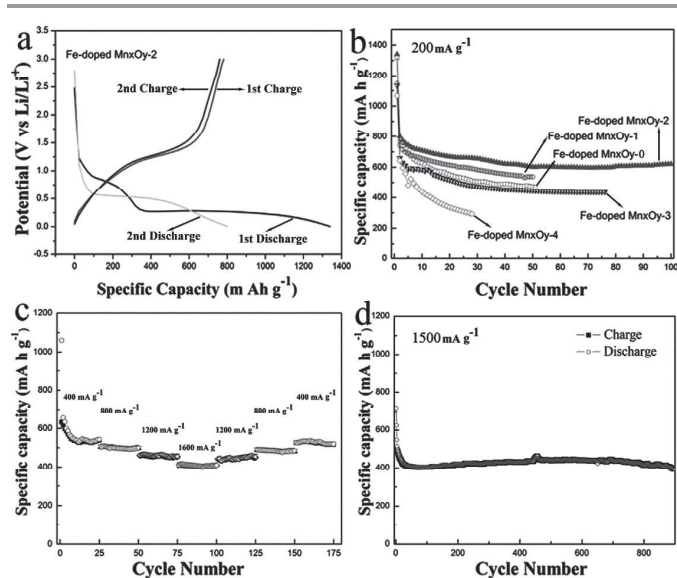


Fig. 13 (a) The 1st and 2nd discharge-charge curves of Fe-doped Mn_3O_4 -2 electrode; (b) Cycle stability of Fe-doped Mn_3O_4 -0, Fe-doped Mn_3O_4 -1, Fe-doped Mn_3O_4 -2, Fe-doped Mn_3O_4 -3 and Fe-doped Mn_3O_4 -4 measured at 200 mA g^{-1} ; (c) Cycling stability of Fe-doped Mn_3O_4 -2 at different current densities; and (d) Cycling performance of Fe-doped Mn_3O_4 -2 at 1500 mA g^{-1} . Reproduced with permission.⁸⁷ Copyright 2013, Wiley.

two-step solution-phase synthesis route to form hybrid materials of Mn_3O_4 nanoparticles with diameters around 10-20 nm on 10wt% reduced graphene oxide (RGO) sheets (Fig. 14). A stable capacity of $\sim 900 \text{ mA} \cdot \text{h g}^{-1}$ ($\sim 810 \text{ mA} \cdot \text{h g}^{-1}$ based on the total mass of the composite) was obtained for the first five cycles when cycled at a current of 40 mA g^{-1} in the voltage range of 0.1–3.0 V vs Li/Li⁺. Very good rate capability and cycling stability were observed. For example, a capacity of $\sim 720 \text{ mA} \cdot \text{h g}^{-1}$ at 400 mA g^{-1} was retained after 40 cycles of charge/discharge at various C-rates. However, the bare Mn_3O_4 nanoparticles exhibit very inferior electrochemical performance, with an initial reversible specific capacity of $300 \text{ mA} \cdot \text{h g}^{-1}$ at 40 mA g^{-1} . The high capacity, good rate capability and cycling stability of this Mn_3O_4 /RGO hybrid material are attributed to the intimate synthesized nanocomposites of Mn_3O_4 (20 nm in diameter) wrapped in graphene sheets (GSs) via a facile, effective, energy-saving, and scalable microwave hydrothermal technique. The composite shows a high specific capacity of more than 900 mAh g^{-1} at 40 mA g^{-1} , and excellent cycling stability with nearly no capacity decay can be observed up to 50 cycles. They firstly give evidence that there is charge transfer between the graphene and the Mn_3O_4 nanoparticles by theoretical calculations. Li *et al.*⁹⁵ developed a facile one-step route to provide interactions between the graphene substrates and the Mn_3O_4 nanoparticles which directly grow on them, which making Mn_3O_4 electrochemically active since charge carriers can be effectively and rapidly conducted back and forth from the Mn_3O_4 nanoparticles to the current collector through the highly conducting three-dimensional graphene network. In addition, the graphene-nanoparticle interactions afford good dispersion of Mn_3O_4 nanoparticles on the RGO sheets which could avoid aggregations of Mn_3O_4 nanoparticles, leading to

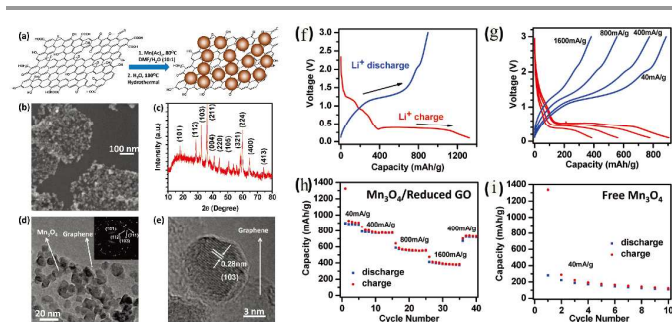


Fig. 14 (a) Schematic two-step synthesis of $\text{Mn}_3\text{O}_4/\text{RGO}$; (b) SEM image of $\text{Mn}_3\text{O}_4/\text{RGO}$ hybrid; (c) XRD spectrum of a packed thick film of $\text{Mn}_3\text{O}_4/\text{RGO}$; (d) TEM image of $\text{Mn}_3\text{O}_4/\text{RGO}$; inset shows the electron diffraction pattern of the Mn_3O_4 nanoparticles on RGO; (e) High-resolution TEM image of an individual Mn_3O_4 nanoparticle on RGO; (f) Charge (red) and discharge (blue) curves of $\text{Mn}_3\text{O}_4/\text{RGO}$ for the first cycle at a current density of 40 mA g^{-1} ; (g) Representative charge (red) and discharge (blue) curves of $\text{Mn}_3\text{O}_4/\text{RGO}$ at various current densities; (h) Capacity retention of $\text{Mn}_3\text{O}_4/\text{RGO}$ at various current densities and (i) Capacity retention of free Mn_3O_4 nanoparticles without graphene at a current density of 40 mA g^{-1} . Reproduced with permission.⁹¹ Copyright 2010, ACS.

better cycle stability. This growth-on-graphene approach offers a new technique for the design and synthesis of high performance anode materials based on highly insulating Mn_3O_4 material. After this work, $\text{Mn}_3\text{O}_4/\text{carbon}$ -based hybrid materials have been intensively studied because of their potential for improving their cycle stability and rate performance as anode materials for LIBs. The specific capacity value and cycling performance were listed in Table 3.⁹²⁻¹⁰¹ For example, Li *et al.*⁹³ successfully synthesized three-dimensional hybrids with Mn_3O_4 nanoparticles homogeneously embedded in the ordered mesoporous carbon (OMC). The $\text{Mn}_3\text{O}_4/\text{OMC}$ hybrids display a high specific capacity up to 802 mA h g^{-1} , and a high coulombic efficiency of up to 99.2% even after 50 cycles at a high current density of 100 mA g^{-1} , revealing its good rate capability and cycling stability. This value is 1.6 times higher than the discharge capacity of 512 mA h g^{-1} for pure ordered OMC materials, and more than 5.4 times higher than the discharge value of 148 mA h g^{-1} for pure Mn_3O_4 nanoparticles. They suggested that the enhanced capacity and cycling performance of the $\text{Mn}_3\text{O}_4/\text{OMC}$ hybrids can be attributed to their unique robust three-dimensional composite structure and the synergistic effects between the Mn_3O_4 nanoparticles and OMC. The ordered mesostructured channels of $\text{Mn}_3\text{O}_4/\text{OMC}$ hybrids are expected to buffer well against the local volume change during the Li uptake/removal reactions and thus to enhance the structural stability. The OMC matrix wall with a thickness of $<10 \text{ nm}$ greatly reduces the solid-state transport length for Li diffusion. Moreover, the hierarchical ordered mesoporosity facilitates the liquid electrolyte diffusion into the bulk of the electrode material and hence provides fast conductive ion transport channels for the conductive Li^+ ions. The improved cycling performance can also be mainly attributed to good electrical contact between the Mn_3O_4 and OMC in the three-dimensional nanocomposites during phase transformation of Mn_3O_4 upon lithiation/delithiation that usually leads to capacity fading. Wang *et al.*⁹⁷ developed a

facile one-step solvothermal reaction route for large-scale synthesis of carbon homogeneously wrapped manganese oxide ($\text{Mn}_3\text{O}_4@\text{C}$) nanocomposites for anode materials, using manganese acetate monohydrate and polyvinylpyrrolidone as precursors and reactants. The synthesized tetragonal structure Mn_3O_4 (space group I41/amd) samples display nanorod-like morphology, with a width of 200–300 nm and a thickness of 15–20 nm. The $\text{Mn}_3\text{O}_4@\text{C}$ nanocomposites display enhanced capacity retention on charge/discharge cycling, with a stable specific capacity of 473 mA h g^{-1} after 50 cycles (as much 3.05 times as that of pure Mn_3O_4 sample). Wang *et al.*⁹⁹ fabricated colloidal Mn_3O_4 nanocrystals supported by graphene oxide (GO) and reduced graphene oxide (RGO) ($\text{Mn}_3\text{O}_4/\text{GO}$ and $\text{Mn}_3\text{O}_4/\text{RGO}$ nanocomposites) through a facile ultrasonic-assisted synthetic route in ethanol amine (ETA)-water system (Fig. 15a). The integration of GO with abundant O-containing groups and the colloidal Mn_3O_4 crystals enable such composite to possess excellent electrochemical performances including high reversible capacity, good cycle stability, and high rate performance that are more suitable to use as the electrode material for electrochemical capacitors (ECs). Comparing with $\text{Mn}_3\text{O}_4/\text{GO}$ nanocomposite, $\text{Mn}_3\text{O}_4/\text{RGO}$ exhibits excellent electrochemical performance in rechargeable LIBs due to the high electrical conductivity of RGOs and the structure of Mn_3O_4 nanocrystals enwrapped in RGOs (Fig. 15b). In addition, they firstly explain how the synergistic compositing structure of $\text{Mn}_3\text{O}_4/\text{GO}$ and $\text{Mn}_3\text{O}_4/\text{RGO}$ nanocomposites plays a very important role in their properties for ECs or LIBs (Fig. 15c). Luo *et al.*¹⁰⁰ recently reported the Li cycling behavior of Mn_3O_4 -carbon nanotubes hybrid material, which is a composite of Mn_3O_4 nanoparticles anchored on continuous super-aligned carbon nanotube (SACNT) films. They reported that the electrochemical performance of the $\text{Mn}_3\text{O}_4/\text{SACNT}$ composite electrode is significantly affected by the content and particle

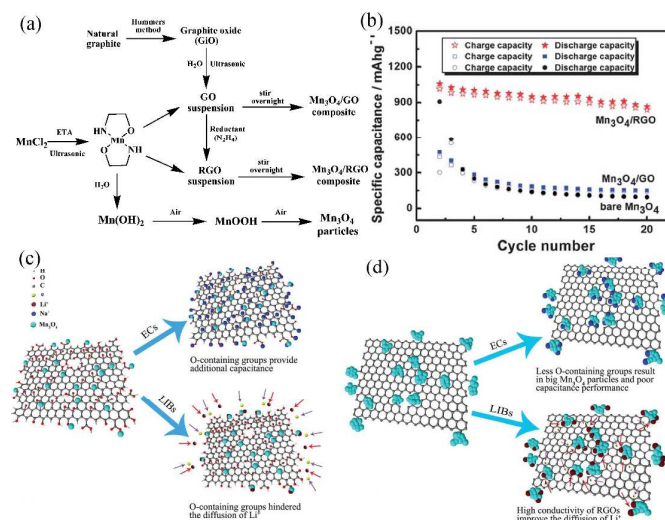


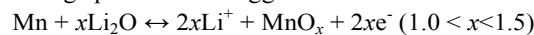
Fig. 15 (a) Preparation routes of Mn_3O_4 nanoparticles, $\text{Mn}_3\text{O}_4/\text{GO}$ and $\text{Mn}_3\text{O}_4/\text{RGO}$ nanocomposites. (b) Cycling performance of these samples at 40 mA^{-1} ; (c) The charge mechanism of $\text{Mn}_3\text{O}_4/\text{GO}$; and (d) $\text{Mn}_3\text{O}_4/\text{RGO}$ for ECs and LIBs. Reproduced with permission.⁹⁹ Copyright 2013, RSC.

size of Mn_3O_4 . It was found that the $\text{Mn}_3\text{O}_4/\text{SACNT}$ composites with size of Mn_3O_4 less than 10 nm demonstrated higher capacity, less extent of polarization, and better cycle stability than the $\text{Mn}_3\text{O}_4/\text{SACNT}$ composite with size of Mn_3O_4 at 165 nm. The optimized $\text{Mn}_3\text{O}_4/\text{SACNT}$ composite displays a capacity of more than 700 mAh g^{-1} at 0.1 C (based on the total mass of the electrode). A large capacity of 342 mAh g^{-1} can still be obtained at a high rate of 10 C, and a capacity retention of 95% was achieved for 100 cycles at 1 C. Despite improvements on the anodic properties of Mn_3O_4 by conductive coating/composites, further studies on the effect of conductive coating on the cycling stability and rate performance still needed to be conducted in the future.

2.3 Mn_2O_3 and its nanocomposites

There were only few reports on Mn_2O_3 nanomaterial based anodes for LIBs before 2010.^{102,103} Liu *et al.*¹⁰² reported preliminary studies of Li cycling behaviors on Mn_2O_3 and found a first discharge and charge capacity of 1080 and 480 mAh g^{-1} , respectively, in the voltage range of $0.2\text{--}3.0 \text{ V}$ vs. Li/Li^+ at 0.25 mA cm^{-2} . Lavela *et al.*¹⁰³ prepared Mn_2O_3 by sol-gel method followed by heat treatment at different temperatures. They reported that Mn_2O_3 showed a discharge potential (1st cycle) at $\sim 0.25 \text{ V}$ vs. Li/Li^+ . The Mn_2O_3 delivered reversible capacities of $500\text{--}700 \text{ mA h g}^{-1}$ depending on the synthesis temperature, when cycled in the voltage range of $0.005\text{--}3.0 \text{ V}$ vs. Li/Li^+ . However, capacity fading was noted in all cases with capacities ranging from 250 to 400 mAh g^{-1} after 20 cycles. Porous one-dimensional Mn_2O_3 nanostructures, containing nanofibers, nanowires and nanorods, were successfully fabricated via a facile hydrothermal treatment and sequential thermal decomposition without any template or surfactant.¹⁰⁴ The as-prepared porous Mn_2O_3 nanofibers, nanorods and nanowires manifested high initial capacities. However, capacity fading was also observed in all cases with capacities of $\sim 250 \text{ mA h g}^{-1}$ after 30 cycles. Similar phenomenon was also found by Shen's group¹⁰⁵ By means of morphology-conserved transformation, Qiu *et al.*¹⁰⁶ synthesized hierarchically structured Mn_2O_3 nanomaterials with different morphologies (oval-shaped and straw-sheaf-shaped) and pore structures by hydrothermal method followed by heating of the products in air at $600 \text{ }^\circ\text{C}$. Both of the as-prepared mesoporous Mn_2O_3 nanomaterials deliver high reversible capacities and excellent cycling stabilities compared to the commercial Mn_2O_3 nanoparticles. They observed a reversible capacity of 380 and $320 \text{ mA}\cdot\text{h g}^{-1}$, respectively, at the end of the 150th cycle for straw-sheaf- and oval-shaped nanostructured Mn_2O_3 at a current of 200 mA g^{-1} when cycled in the voltage range of $0.01\text{--}2.5 \text{ V}$ vs. Li/Li^+ . Moreover, they suggested that the good capacity retention capability of the straw-sheaf-shaped Mn_2O_3 is due to the relatively high surface area and the peculiar nanostrip structure, resulting in the reduced length for lithium ion diffusion. Recently, our group¹⁰⁷ have synthesized porous Mn_2O_3 microspheres by morphology-controlled decomposition of spherical MnCO_3 precursors at $600 \text{ }^\circ\text{C}$. The porous Mn_2O_3

microspheres show a specific capacity as high as 796 mAh g^{-1} at a current density of 100 mA g^{-1} after 50 cycles. In addition, a high rate performance ($\sim 600 \text{ mA h g}^{-1}$ at 1200 mA g^{-1}) was also observed. Based on the CV curves, the discharge-charge curves and the ex-situ XRD analysis, a novel lithium storage mechanism of the synthesized porous Mn_2O_3 material after the first discharge process was suggested as follows:



After our work, porous Mn_2O_3 hierarchical microspheres^{108, 109} Mn_2O_3 nanocones,¹¹⁰ polyhedrons,¹¹¹ porous sheets,¹¹² cubic and spindle¹¹³ have been synthesized and investigated as anode materials by other groups. All of these results were listed in Table 4. Although some advance have been made in Mn_2O_3 anode materials via the morphology optimization, further studies on the improvement of the cycling stability and rate performance are still required.

[Table 4]

A recent good report of Cu-doped hollow spherical Mn_2O_3 sample by Li *et al.*¹¹³ showed a higher specific capacity of 642 mAh g^{-1} at a current density of 100 mA g^{-1} after 100 cycles. They suggested that the significant enhancement of the electrochemical lithium storage performance can be attributed to the improvements of the electronic conductivity and lithium diffusivity of electrodes.

Xia's group¹¹⁴ prepared Mn_2O_3 nanowires by thermal annealing of MnOOH nanowires precursor, which was transformed from hydrothermally grown MnO_2 nanoflakes and directly attached on Ti foils via reaction with poly(vinyl pyrrolidone) (Fig. 16a). The Mn_2O_3 nanowires (Fig. 16b) show an initial discharge capacity of $815.9 \text{ mA h g}^{-1}$ at 100 mA g^{-1} and maintains a capacity of $502.3 \text{ mA h g}^{-1}$ after 100 cycles (Fig. 16c), and good rate performance of 220 mAh g^{-1} at 1000 mA g^{-1} (Fig. 16d). Furthermore, they firstly fabricated a flexible $\text{Mn}_2\text{O}_3/\text{LiMn}_2\text{O}_4$ lithium ion full cell using the Mn_2O_3 nanowires as anode and LiMn_2O_4 nanowires as cathode, respectively (Fig. 17). The full cell has an output voltage of >3

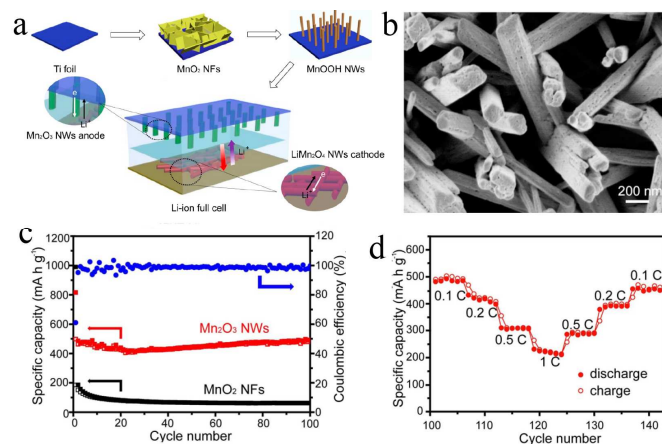


Fig. 16 (a) Schematic of the synthesis of the Mn_2O_3 nanowires (NWs) and fabrication the $\text{Mn}_2\text{O}_3/\text{LiMn}_2\text{O}_4$ LIB full cell; (b) SEM images of Mn_2O_3 NWs grown on Ti foils; (c) Cycling performance of Mn_2O_3 NWs (red curve) for the first 100 cycles; and (d) Rate performance of Mn_2O_3 NWs (1C = 1000 mA g^{-1}). Reproduced with permission.¹¹⁴ Copyright 2013, ACS.

V, low thickness of 0.3 mm, high flexibility, and a specific capacity of 99 mA h g^{-1} based on the total weight of the cathode material. It also exhibits good cycling stability with a capacity of $\sim 80 \text{ mA h g}^{-1}$ after 40 charge/discharge cycles. This successful example of the $\text{Mn}_2\text{O}_3/\text{LiMn}_2\text{O}_4$ full cell and further optimization and development of the nanowire design and fabrication will lead to new opportunities of high power-density energy storage devices.

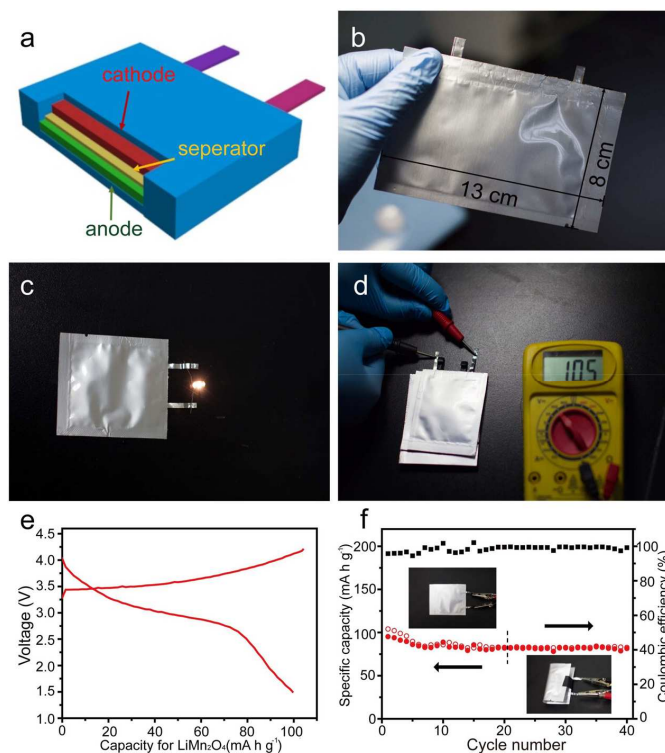


Fig. 17 Flexible $\text{Mn}_2\text{O}_3/\text{LiMn}_2\text{O}_4$ full cells. (a) 3D structure scheme and (b) optical image of a flexible $\text{Mn}_2\text{O}_3/\text{LiMn}_2\text{O}_4$ full cell; (c) Optical images showing a light emitting diode (3 V, 10 mW) powered by a flexible $\text{Mn}_2\text{O}_3/\text{LiMn}_2\text{O}_4$ full cell; (d) Optical image of the voltage output of a three-cell battery in tandem; (e) Charge/discharge curves of a flexible $\text{Mn}_2\text{O}_3/\text{LiMn}_2\text{O}_4$ full cell at the first cycle and (f) Cycling performance (red curve) and Coulombic efficiency (black curve) of a representative flexible $\text{Mn}_2\text{O}_3/\text{LiMn}_2\text{O}_4$ full cell. Reproduced with permission.¹¹⁴ Copyright 2013, ACS.

2.4 MnO_2 and its nanocomposites

Manganese dioxide (MnO_2) possesses a high theoretical capacity of 1233 mAh g^{-1} based on the conversion mechanism.^{44, 115} Moreover, it is of environmental benignity and natural abundance. This makes it a promising material for applications in lithium ion batteries. However, due to the low conductivity of MnO_2 and large volume expansion during battery operation, rather low coulombic efficiencies in the first cycle and rapid capacity decays with cycling were obtained.¹¹⁶⁻¹¹⁹ For example, Li *et al.*¹¹⁷ synthesized novel α - MnO_2 hollow urchins on a large scale by a facile and efficient low-temperature (60°C) mild reduction route. The α - MnO_2 hollow urchins show a high capacity of 746.0 mAh g^{-1} in the first discharge process, but the capacity of the 40th cycle is only 481 mAh g^{-1} , about 64.4% of the initial capacity. As reported by Reddy *et al.*,¹¹⁹ a coaxial MnO_2/CNT array material can give an initial capacity of

around 2000 mAh g^{-1} at a rate of 50 mA g^{-1} . However, the capacity is sharply decayed to 500 mA h g^{-1} after only 15 cycles. They suggested the initial high capacity and enhanced lithium storage capacity can be attributed to *in-situ* deposition of MnO_2 on CNTs, while the fast capacity decay might result from a structural deterioration of a thick layer of MnO_2 with a compact structure deposited on the outside surface of CNTs. One of the best results showing a capacity of 600 mAh g^{-1} after 100 cycles for a γ - MnO_2 film deposited on nickel metal was reported before 2010.¹¹⁸ Notwithstanding these results, systematic efforts have been dedicated to optimize the MnO_2 electrodes by combining materials synthesis, processing and engineering techniques, so as to improve the electrochemical performance.

Attempts have also been made recently to fabricate MnO_2 composites with unique nanostructures,¹²⁰⁻¹²² MnO_2 -based nanocomposites consisting of MnO_2 nanostructures and electrically conductive carbon such as carbon nanotubes¹²³⁻¹²⁵ amorphous carbon¹²⁶ or graphene,¹²⁷⁻¹³¹ its nanocomposites including MnO_2 and other transition metal oxides,¹³²⁻¹³⁴ and MnO_2 @polymers.¹³⁵ All of these relative results are listed in Table 5. Kundu *et al.*¹³² report the direct growth of mesoporous MnO_2 nanosheet (NS) arrays on a nickel (Ni) foam current collector by electro-deposition followed by a low temperature thermal annealing process (170°C) in a nitrogen atmosphere. When using the Ni foam supported mesoporous MnO_2 NS arrays as an anode in LIBs, they found that the electrode can deliver a reversible capacity as high as 1690 mA h g^{-1} even after 100 cycles at a charge–discharge current density of 100 mA g^{-1} . Two anodic peaks located at 1.3 and 2.4 V vs Li/Li^+ are observed, and they suggested that the re-oxidation of manganese may take place in two steps. It is also interesting to note that the capacity gradually increases with the increasing cycle numbers, which is opposite to the previous literatures.^{116-120,135} It is assumed that the increase in capacity might originate from the increased number of vacancies and grain boundaries due to the pulverization of the MnO_2 NSs upon cycling, where Li ions could be stored. This example suggests the electrochemical performance of MnO_2 may be optimized by nanostructure tuning. Guo *et al.*¹²⁷ reported a novel approach to fabricate a hierarchically nanostructured composite comprising one-dimensional (1-D) rod-like layered birnessite-type manganese oxide (LMO), 2-D graphene nanosheets, and a 3-D porous structure (LMO/PEDOT/graphene). As shown in Fig. 18a, the 3-D graphene material is used as a supporting matrix, on which *in situ* polymerized poly(3,4-ethylenedioxythiophene) (PEDOT) is assembled for the direct growth of uniformly distributed 1-D rod-like LMOs. The composites exhibit a large first discharge capacity of 1835 mAh g^{-1} , a reversible discharge capacity of 1105 mA h g^{-1} and 948 mA h g^{-1} after 15 cycles at a rate of 50 mA g^{-1} (Fig. 18b and 18c). They suggested that the performance enhancement of the LMO/PEDOT/graphene in lithium ion batteries can be explained as follows: (1) the LMO in LMO/PEDOT/graphene has characteristics of an open structure with an interlayer space of approximately 7.2 \AA to promote efficient lithium intercalation/deintercalation for high specific capacity; (2) the use of highly conductive 3-D graphene material is favorable in electron transport to enable a fast charge/discharge rate and (3) the PEDOT coating directs the growth of relatively ordered textured LMO and prevents its aggregation for

uniform distribution, which can accommodate large volume expansion during battery operation.

[Table 5]

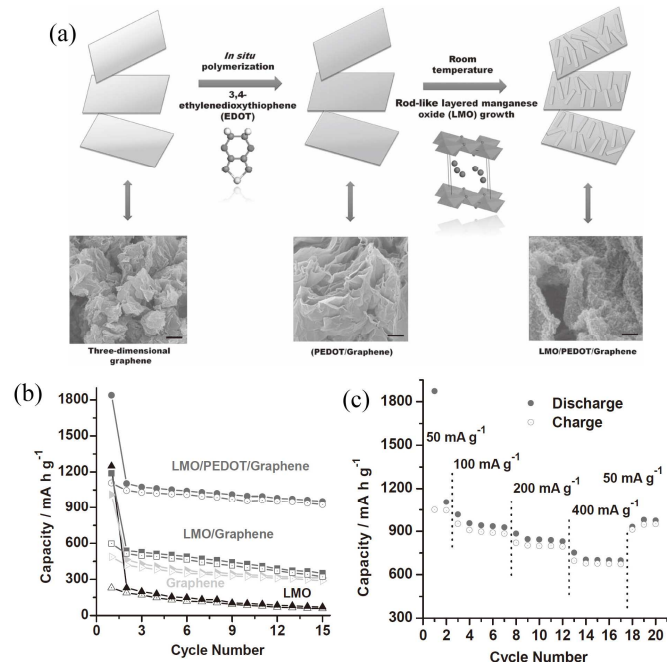


Fig. 18 (a) Schematic representation of the hierarchically nanostructured composite fabrication; (b) Cycling variation in charge/discharge capacity vs. cycle number for different lithium ion batteries; and (c) Capacity of LMO/PEDOT/graphene batteries under various current densities. Reproduced with permission.¹²⁷ Copyright 2011, Wiley.

Li *et al.*¹²⁹ designed a unique hierarchical sandwiched structured graphene–MnO₂–GNRs (GMG) composite in which the graphene wraps the porous MnO₂ that directly grows from graphene nanoribbons (GNRs). Fig. 19a depicted the synthesis procedures of the GMG composites. In the composites, graphene and GNRs are in good contact with MnO₂, improving the electrical conductivity of the GMG composites. More importantly, graphene and GNRs can buffer the volume changes and prevent the loss of MnO₂ during Li ion conversion reaction with Li, improving the composite's electrochemical stability performance. As an anode material, the GMG composites demonstrate a reversible specific discharge capacity of 890 mAh g⁻¹ at 0.1 A g⁻¹ after 180 cycles with various current rates ranging from 0.1 to 1.0 A g⁻¹ and shows about 24% improvement compared to the initial capacity after 245 cycles at a current density of 0.4 A g⁻¹ (Fig. 19b).

In a recent paper, Li *et al.*¹³¹ prepared MnO₂/3D porous graphene-like (PG) (3D PG–xMn) composites via a simple and cost-effective redox process. Typically, the self-controlled reaction between 3D PG and KMnO₄ under neutral pH conditions led to the homogeneous deposition of MnO₂ on the 3D PG networks. They suggested that the porosities of the 3D PG–xMn composites can be adjusted by the initial concentration of KMnO₄. The surface area and total pore volume of 3D PG–MnO₂ on 3D PG, there was no obvious decrease in powder conductivity of the 3D PG–xMn ($x = 0.5$ and 1.0) composites,

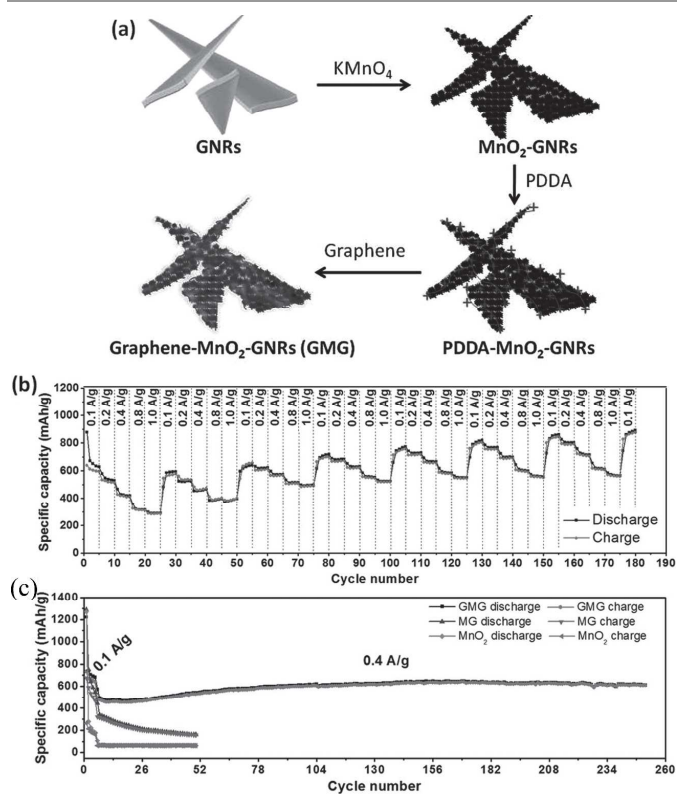


Fig. 19 (a) Schematic illustration of the synthesis of the GMG composite; (b) Rate performance of GMG at various current rates from 0.1 to 1.0 A g⁻¹; and (c) Cycling performance of MnO₂, MG, and GMG at the 0.1 A g⁻¹ for the first five cycles and the 0.4 A g⁻¹ for the following cycles. Reproduced with permission.¹²⁹ Copyright 2013, Wiley.

while the 3D PG–1.5Mn composite shows an obvious decrease. Among the three 3D PG–xMn composites, the 3D PG–1Mn composite displayed the best electrochemical performance. It delivered a discharge capacity of 988 mAh g⁻¹ at the second cycle and the discharge capacity could be retained as high as 836 mAh g⁻¹ after 200th cycle (~84.6% capacity retention). The excellent electrochemical performances of the as-prepared 3D PG–1Mn composites can be attributed to the synergistic effects that stem from its reasonable MnO₂ content (62.7wt% MnO₂) and high conductivity. The branched nanocomposites with β -MnO₂ nanorods as the back-bone and porous α -Fe₂O₃ nanorods as the branches were synthesized by Gu *et al.*¹³² They used a high-temperature annealing process to achieve epitaxial growth of FeOOH on the β -MnO₂ nanorods. The branched nanorods of β -MnO₂/ α -Fe₂O₃ exhibit a reversible specific capacity of 1028 mAh g⁻¹ at a current density of 1000 mA g⁻¹ up to 200 cycles and 881 mAh g⁻¹ at 4000 mA g⁻¹. The presence of α -Fe₂O₃ in the branched nanorods greatly promotes the charge transfer at the electrode/electrolyte interface, which is beneficial to the electrochemical performance. These results indicate the importance of the selection of proper chemical xMn composites gradually decrease with the increase of the concentration of KMnO₄. The combination of the advantages in structure and components would effectively improve the performance of electrode materials in LIBs.

3. Ternary Mn-based Oxides as anode materials

Ternary Mn-based oxides containing AMn_2O_4 ($A = \text{Co}$ and Zn) with a spinel or spinel-like crystal structure have been investigated as anode materials for LIBs. The Li cycling mechanism involves the “alloying and conversion reaction” for ZnMn_2O_4 and the “conversion reaction” for CoMn_2O_4 .⁸ Depending on the structure, morphology, particle size and composition, large and stable reversible capacities have been reported.

3.1 ZnMn_2O_4 -based anodes

ZnMn_2O_4 has been proposed as a practical alternative anode material for LIBs because of its high theoretical capacity of 1008 mAh g^{-1} (the Zn metal can form an alloy with Li and participate in the conversion reaction along with manganese), low oxidation potentials (*i.e.*, delithiation potential) of zinc and manganese at 1.2 and 1.5 V vs. Li/Li^+ , respectively. These low oxidation potentials could eventually increase the battery output voltage compared to ZnFe_2O_4 , and ZnCo_2O_4 , allowing higher energy density delivery. Furthermore, zinc and manganese are abundant, environmentally friendly, and relatively inexpensive compared to cobalt.^{45, 136}

Yang *et al.*⁴⁵ synthesized ZnMn_2O_4 nanocrystals by a polymer pyrolysis method and first used the obtained nanocrystals as lithium storage anode materials. The nanocrystalline ZnMn_2O_4 electrode delivers an initial reversible capacity of 766 mAh g^{-1} when cycled at 100 mA g^{-1} in the voltage range of 0.01–3.0 V vs. Li/Li^+ . Cycling studies up to 50 cycles show almost stable cycling performance between 10 and 50 cycles with only an average capacity fading of 0.20% per cycle and the electrode still maintains a capacity of 569 mAh g^{-1} after 50 cycles. After that, ZnMn_2O_4 with different particle size and morphologies including flower-like ZnMn_2O_4 superstructures,¹³⁶ ZnMn_2O_4 nanoparticles,^{44, 137, 138} ZnMn_2O_4 nanowires,¹³⁹ ZnMn_2O_4 nanoplates,¹⁴⁰ ZnMn_2O_4 hollow microspheres,^{141–143} ball-in-ball ZnMn_2O_4 hollow microspheres,¹⁴⁴ loaf-like ZnMn_2O_4 nanorods,¹⁴⁵ ZnMn_2O_4 nanofibers¹⁴⁶ and ZnMn_2O_4 mesoscale tubular arrays¹⁴⁷ have been studied and applied as anode materials for LIBs. All of the corresponding results are listed in Table 6. Specifically, the ball-in-ball ZnMn_2O_4 hollow microspheres¹⁴³ were prepared by a novel template-free method (Fig. 20a–d). The hollow microspheres typically consist of small nanoparticles with an average size of 30 nm, and exhibit a mesoporous feature. When used as an anode material for LIBs, the ZnMn_2O_4 hollow microspheres show a high specific capacity of 750 mAh g^{-1} after 120 cycles at 400 mA g^{-1} (Fig. 20e and f). Despite the improved cyclic and rate performance of the ZnMn_2O_4 nanomaterials obtained by different strategies, further studies are still required to achieve the long cycling stability and the high rate performance of these materials.

[Table 6]

Recently, in an attempt to improve the electrochemical properties of ZnMn_2O_4 , Zheng *et al.*¹⁴⁸ prepared thermally reduced graphene oxide (rGO)-wrapped ZnMn_2O_4 nanorods via a facile bottom-up approach. They suggested that this unique architecture can provide 1D interconnected ZnMn_2O_4 nanoparticle networks to facilitate rapid

diffusion of lithium ions within the electrode material. Meanwhile, the rGO sheets could act as a conductive layer for electron transfer and an efficient buffer layer to enable the structural stabilization of ZnMn_2O_4 crystals. As the results, a high and stable reversible capacity (707 mA h g^{-1} at 100 mA g^{-1} over 50 cycles) and an excellent rate capability (440 mA h g^{-1} at 2000 mA g^{-1}) are achieved with this composite.

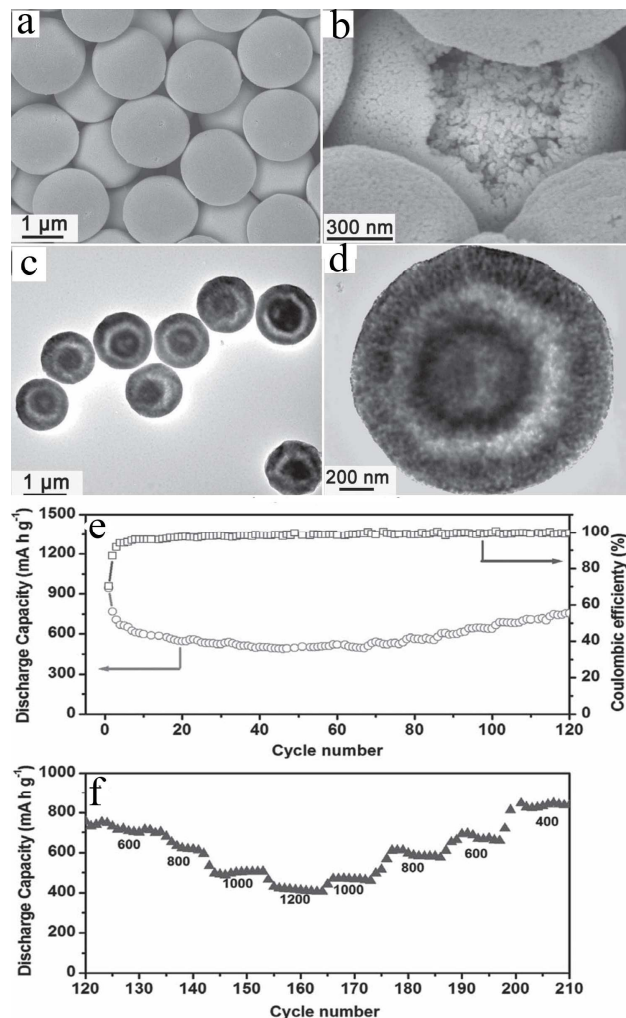


Fig. 20 Typical (a), (b) FESEM and (c), (d) TEM images of ZnMn_2O_4 ball-in-ball hollow microspheres; (e) Cycling performance of the ZnMn_2O_4 hollow microspheres in the voltage range of 0.01–3.0 V vs. Li/Li^+ at current densities of 400 mA g^{-1} and rate performance at different current densities for the same cell after 120 cycles. Reproduced with permission.¹⁴³ Copyright 2012, Wiley.

As mentioned in the introduction section, the reasonable selections of binders and electrolyte are beneficial to the improvement of the rate and cyclic performance of metal oxides-based electrodes. Courtel *et al.*⁴⁴ have studied the effects of the binder and electrolyte on the cycling performance of ZnMn_2O_4 in a recently published paper. The electrochemical performance of ZnMn_2O_4 electrodes using five binders (PVDF dissolved in NMP, and four other water-soluble binders such as NaCMC, LiCMC, XG and Baytron; CMC = carboxymethylcellulose) show that the LiCMC and NaCMC are

the best binders (Fig. 21). Specifically, the electrode fabricated by ZnMn_2O_4 nanoparticles (<150 nm) sintered at 800 °C and LiCMC binder exhibit a capacity of 690 mA h g^{-1} after 70 cycles at C/10 and good rate capability (450 mA h g^{-1} for 0.5C, 340 mA h g^{-1} for 1 C, 230 mA h g^{-1} for 2C, and 150 mA h g^{-1} for 3C rate, respectively). In addition, studies on the effect of the electrolyte on the cycling performance of ZnMn_2O_4 electrode showed that carbonate (EC) : dimethyl carbonate (DEC) mixture (3:7 by vol.) is the best electrolyte and the PC (propylene carbonate) is the worst one (Fig. 22). These results could be explained by the fact that PC does not form the polymeric organic layer or that the layer formed with PC is

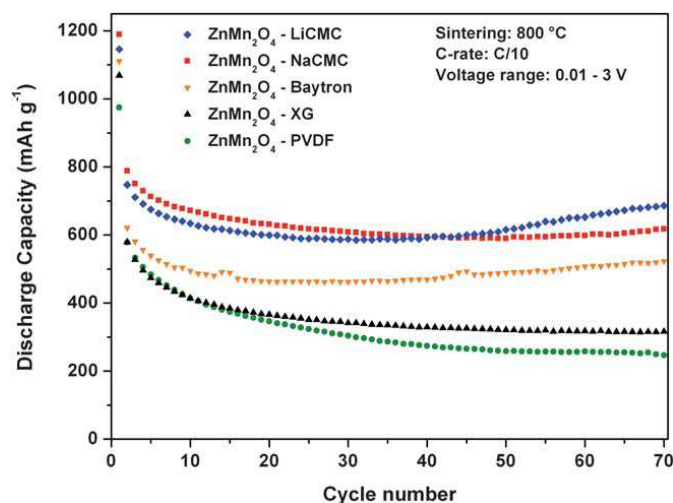


Fig. 21 Discharge capacities of ZnMn_2O_4 electrodes made using five different binders: PVDF, NaCMC, LiCMC, XG, and Baytron. Reproduced with permission.⁴⁴ Copyright 2011, RSC.

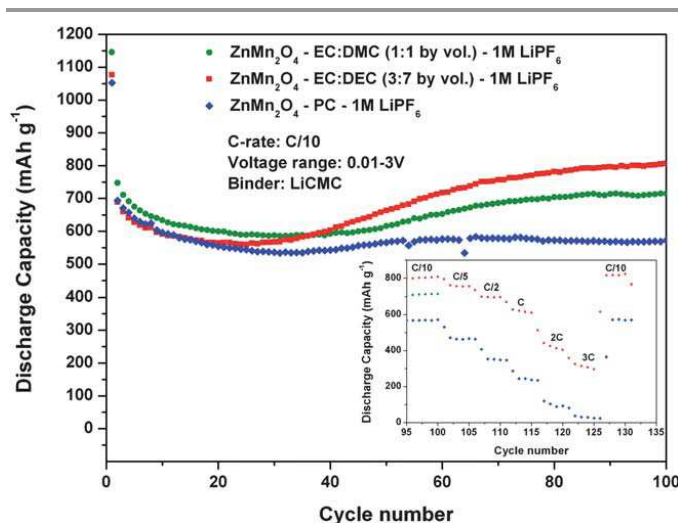


Fig. 22 Discharge capacities of ZnMn_2O_4 electrodes. The cells were cycled at room temperature using the same lithium salt, 1 M LiPF_6 in three different electrolytes: EC : DMC (1 : 1 by vol.), EC : DEC (3 : 7 by vol.), and PC. Reproduced with permission.²¹ Copyright 2011, RSC.

inactive to lithium storage. Furthermore, the authors assembled a full cell for the first time, using ZnMn_2O_4 as an anode material, $\text{LiMn}_{1.5}\text{Ni}_{0.5}\text{O}_4$ as cathode material, and 1 M LiPF_6 in

EC : DEC (3:7 by vol.) as electrolyte. The full cell was cycled between 1.5 V and 4.7 V at 0.1 C and the capacity was reported versus the limiting electrode (cathode). The initial capacity at a cycling rate of 0.1 C is 108 mAh g^{-1} . During the first charge there is a plateau at 4.1 V. However, in the subsequent discharge and charge cycles, the charge vs. voltage curve exhibits a sloping voltage between 3.5 V and 3 V and 3.5 and 4.1 V, respectively. Unfortunately, after 20 cycles, the battery only exhibits a capacity of 75 mAh g^{-1} .

3.2 CoMn_2O_4 anodes

CoMn_2O_4 has an incomplete normal-type spinel with a tetragonal structure ($c/a = 1.14$) because of the Jahn–Teller effect of Mn^{3+} ($3d^4$). Co^{2+} mainly occupies the A sites and Mn^{3+} mainly occupies the B sites. It can store Li^+ through the oxidation of metallic Co and Mn to CoO and MnO respectively, leading to a high initial discharge capacity of 921 mA h g^{-1} and a reversible capacity of 691 mAh g^{-1} .^{44, 149} Courtel *et al.*⁴⁴ first reported sub-micrometer sized CoMn_2O_4 particles with a reversible capacity of about 515 mAh g^{-1} at a current density of 69 mA g^{-1} . However, a capacity of only 330 mAh g^{-1} after 50 cycles was obtained for this material.

Investigation conducted by Zhou *et al.*¹⁵⁰ on double-shelled CoMn_2O_4 hollow microcubes prepared via a facile coprecipitation and annealing method (600 °C with a ramping rate of 2 °C min^{-1}) using $\text{Co}_{0.33}\text{Mn}_{0.67}\text{CO}_3$ as precursor, showed an initial discharge and charge capacities of 1282 and 806 mA h g^{-1} and a reversible capacity of 624 mAh g^{-1} after 50 cycles at 200 mA g^{-1} , respectively (Fig. 23). It is interesting that the initial charge capacity is much higher than the theoretical value (691 mAh g^{-1}) based on the oxidation reactions of metallic Co and Mn nanoparticles to CoO and MnO: $3\text{Li}_2\text{O} + \text{Co} + 2\text{Mn} \leftrightarrow 2\text{MnO} + \text{CoO} + 6\text{Li}^+ + 6\text{e}^-$. They suggested that the extra reversible capacity in their studies is attributed to the reversible formation/dissolution of polymeric gel-like film. Single-crystalline CoMn_2O_4 nano/submicrorods with diameters of about 100 nm and lengths up to tens of micrometers were synthesized¹⁵¹ by using hydrothermally synthesized $\beta\text{-MnO}_2$ nanorods as the templates and cobalt hydroxide as cobalt source followed by annealing at 650 °C in air for 10 h with a heating rate of 5 °C min^{-1} . The reversible capacities of 512 and 400 mAh g^{-1} at the current densities of 200 and 1000 mA g^{-1} after 100 cycles were obtained, respectively, in their report. Recently, Kim *et al.*¹⁵² synthesized yolk–shell and hollow CoMn_2O_4 powders by spray pyrolysis from aqueous spray solutions of the cobalt and manganese components with different concentrations of sucrose. The single and double-shelled yolk–shell powders prepared from spray solutions with 0.4 and 0.7 M sucrose have high discharge capacities of 519 and 573 mAh g^{-1} in the voltage range of 0.01–3 V vs. Li/Li^+ , respectively, after 40 cycles at a high discharge rate of 800 mA g^{-1} . The group of Lou¹⁵³ obtained hierarchical CoMn_2O_4 array micro/nanostructures with tunable morphology on conductive stainless steel by a facile solvothermal route and a subsequent annealing treatment. The CoMn_2O_4 nanowires show reversible

capacities of 530–215 mA h g⁻¹ when cycled at 1–10 C (1 C = 700 mA g⁻¹). Additional recent studies on CoMn₂O₄ as anode materials are multiporous CoMn₂O₄ spinel quasi-hollow spheres reported by Li *et al.*¹⁵⁴ and hierarchical nanosheets reported by Hu *et al.*¹⁵⁵

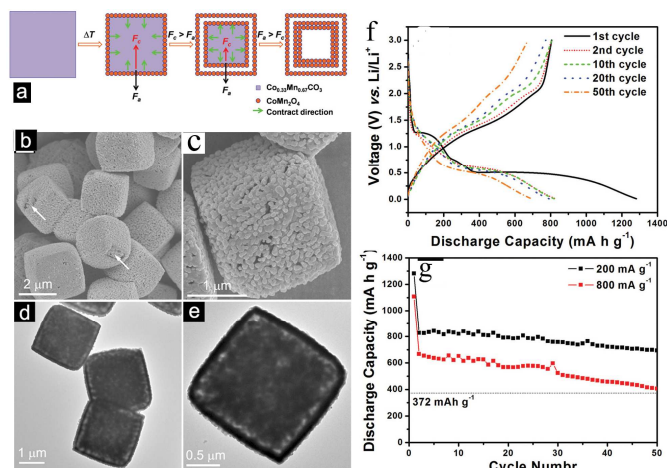


Fig. 23 (a) Illustration of the fabrication of double-shell CoMn₂O₄ hollow microcubes; Typical (b), (c) FESEM and (d), (e) TEM images; (f) discharge/charge profiles; and (g) cycling performance of the double-shelled CoMn₂O₄ hollow microcubes in the voltage range of 0.01–3.0 V vs. Li/Li⁺ at current densities of 200 and 800 mA g⁻¹. Reproduced with permission.¹⁵⁰ Copyright 2013, Wiley.

4. Conclusion and Outlook

The progress of design, synthesis and electrochemical evaluation of Li storage and cycling properties of binary, ternary, and complex Mn-based metal oxides in recent years have been reviewed. The motivations of the reviewed studies of these oxides as anode materials came from the eager to replace the graphite anode and increase the energy density, decrease the cost, and improve the safety operation of the existing LIBs.

There are two mechanisms, the “conversion reaction” mechanism for binary Mn-based oxides (MnO, Mn₃O₄, Mn₂O₃ and MnO₂) and some ternary oxides (CoMn₂O₄) as well “conversion reaction involving alloying” mechanism for ZnMn₂O₄. As discussed previously, many strategies including morphology control of the micro-/nanostructures, carbon-coating, composition optimization of the Mn-based oxides have been extensively developed, with the aim to improve the rate and cycling performance and to promote the practical application of these oxides in LIBs. Despite some important advances have been made on the cycling and rate performance of the Mn-based oxides as anode materials, the majority of the literatures regarding the applications of these oxides in LIBs with promising enhancement are mainly experimental results. Furthermore, different experimental results were obtained even if the same synthetic methods were used to prepare Mn-based anode materials with the same morphologies. A comprehensive and in-depth insight into the relationship among the composition, micro/nano-structures and the electrochemical Li storage performance of these oxides are therefore still in imminent demand. This requires *in-situ* characterizations,

including *in-situ* X-ray diffraction (XRD), *in-situ* X-ray absorption spectroscopy (XAS) and *in-situ* high-resolution transmission electron microscopy (HTEM), to verify the fine structure and the reaction pathway of the obtained materials, and to assign electrochemical features with specific reactions.

Because of the large electrode polarization and solid electrolyte interphase (SEI) film formation, the Mn-based oxides suffer from large irreversible capacity loss (ICL) during the first cycle. Moreover, the mechanical and chemical properties of SEI film have significant impacts on the columbic efficiency, the cycling performance and the safety operation of LIBs. Great efforts should be paid to modify the mechanical properties of SEI films by electrolyte additive addition and/or electrode surface modification, aiming at the formation of elastic and flexible SEI films to accommodate large volume variation during charging/discharging cycles and achieve excellent cycling performance and high columbic efficiencies.

The fabrication of full cells using Mn-based oxides as anode materials has been rarely investigated, although several examples have been reported in recent years. The Mn-based oxides are suitable to assemble full cells by combining with 4 V and 5 V cathodes. To obtain full cells with high cycling and rate performance as well as good safety, significant developments need to be made on the optimization of the preparation parameters of the anodes, cathodes and electrolytes as well their matching. It will boost the development of full cells based on the Mn-based oxides as anode materials in the coming years.

In spite of the challenges aforementioned, the field for the research of Mn-based oxide anodes, especially for MnO, Mn₃O₄ and ZnMn₂O₄, for LIBs has a very bright future due to the extensive applications of nanotechnology and *in-situ* characterization techniques.

Acknowledgements

This work was supported by the special financial grant from the China postdoctoral science foundation (2013T60795), the Guangzhou Scientific and Technological Planning Project (2013J4100112), the Guangdong Province Science & Technology Bureau (Industry-Education-Research Project, grant no. 2011B050300008, 2012B050300004), and the Fok Ying Tung Foundation (NRC07/08.EG01).

Notes and references

- ^a The Key Laboratory of Fuel Cell Technology of Guangdong Province, School of Chemistry and Chemical Engineering, South China University of Technology, Guangzhou, China. E-mail: chyfdeng@scut.edu.cn
^b Center for Green Products and Processing Technologies, Guangzhou HKUST Fok Ying Tung Research Institute, Guangzhou 511458, China.
^c Department of Chemical and Biomolecular Engineering, The Hong Kong University of Science and Technology, Hong Kong, China.
 Electronic Supplementary Information (ESI) available: [details of any supplementary information available should be included here]. See DOI: 10.1039/b000000x/

- 1 <http://www.isuppli.com/semiconductor-value-chain/pages/strong-growth-to-drive-lithium-ion-battery-market-to-61-billion-by-2020.aspx> (Accessed on Feb. 29, 2012).
- 2 M. G. Kim and J. Cho, *Adv. Funct. Mater.*, 2009, **19**, 1497.
- 3 P. G. Bruce, B. Scrosati and J. M. Tarascon, *Angew. Chem., Int. Ed.*, 2008, **47**, 2930.
- 4 J. M. Tarascon, N. Recham, M. Armand, J. N. Chotard, P. Barpanda, W. Walker and L. Dupont, *Chem. Mater.*, 2010, **22**, 724.
- 5 B. J. Landi, M. J. Ganter, C. D. Cress, R. A. DiLeo and R. P. Raffaele, *Energy Environ. Sci.*, 2009, **2**, 638.
- 6 M. R. Palacin, *Chem. Soc. Rev.*, 2009, **38**, 2565.
- 7 L. W. Ji, Z. Lin, M. Alcoutlabi and X. W. Zhang, *Energy Environ. Sci.*, 2011, **4**, 2682.
- 8 M. V. Reddy, G. V. Subba Rao and B. V. R. Chowdari, *Chem. Rev.*, 2013, **113**, 5364.
- 9 M. Gu, I. Belharouak, J. Zheng, H. Wu, J. Xiao, A. Genc and C. Wang, *ACS Nano.*, 2013, **7**, 760.
- 10 J. Zheng, J. Xiao, X. Yu, L. Kovarik, M. Gu, F. Omenya and J. G. Zhang, *Phys. Chem. Chem. Phys.*, 2012, **14**, 13515.
- 11 M. Gu, I. Belharouak, A. Genc, Z. Wang, D. Wang, K. Amine and C. Wang, *Nano letters*, 2012, **12**, 5186.
- 12 A. Manthiram, K. Chemelewski and E. S. Lee, *Energy Environ. Sci.*, 2014, **7**, 1399.
- 13 M. Winter, J. O. Besenhard, M. E. Spahr and P. Novak, *Adv. Mater.*, 1998, **10**, 725.
- 14 Z. G. Yang, D. Choi, S. Kerisit, K. M. Rosso, D. H. Wang, J. Zhang, G. Graff and J. Liu, *J. Power Sources*, 2009, **192**, 588.
- 15 A. Magasinski, P. Dixon, B. Hertzberg, A. Kvit, J. Ayala and G. Yushin, *Nat. Mater.*, 2010, **9**, 353.
- 16 M. Gu, Y. Li, X. Li, S. Hu, X. Wang, W. Hu and C. Wang, *ACS Nano.*, 2012, **6**(9), 8439.
- 17 M. Gu, Z. Wang, J. G. Connell, D. E. Peaea, L. J. Lauhon, F. Gao and C. Wang, *ACS Nano.*, 2013, **7**(7), 6303.
- 18 R. A. Huggins, *J. Power Sources*, 1999, **81**, 13.
- 19 X. Wen Lou, C. M. Li and L. A. Archer, *Adv. Mater.*, 2009, **21**, 2536.
- 20 J. Y. Huang, L. Zhong, C. M. Wang, J. P. Sullivan, W. Xu, L. Q. Zhang and J. Li, *Science*, 2010, **330**, 1515.
- 21 J. S. Chen and X. W. Lou, *Small*, 2013, **9**, 1877.
- 22 M. Gu, A. Kushima, Y. Shao, J. G. Zhang, J. Liu, N. D. Browning and C. Wang, *Nano letters*, 2013, **13**, 5203.
- 23 R. Wang, C. Xu, J. Sun, L. Gao and H. Yao, *ACS Appl. Mater. Interfaces*, 2014, **6**, 3427.
- 24 D. J. Xue, S. Xin, Y. Yan, K. C. Jiang, Y. X. Yin, Y. G. Guo and L. J. Wan, *J. Am. Chem. Soc.*, 2012, **134**, 2512.
- 25 L. F. Cui, R. Ruffo, C. K. Chan, H. L. Peng and Y. Cui, *Nano Lett.* 2009, **9**, 491.
- 26 M. N. Obrovac, L. Christensen, D. B. Le and J. R. Dahn, *J. Electrochem. Soc.*, 2007, **154**, A849.
- 27 C. M. Park, J. H. Kim, H. Kim and H. J. Sohn, *Chem. Soc. Rev.* 2010, **39**, 3115.
- 28 P. Poizot, S. Laruelle, S. Grugeon, L. Dupont and J. M. Tarascon, *Nature*, 2000, **407**, 496.
- 29 J. Cabana, L. Monconduit, D. Larcher and M. R. Palacin, *Adv. Mater.*, 2010, **22**, E170.
- 30 H. B. Wu, J. S. Chen, H. H. Hng and X. W. Lou, *Nanoscale*, 2012, **4**, 2526.
- 31 H. Wang, H. Dai, *Chem. Soc. Rev.*, 2013, **42**, 3088.
- 32 C. Xu, B. Xu, Y. Gu, Z. Xiong, J. Sun and X. S. Zhao, *Energy Environ. Sci.*, 2013, **6**, 1388.
- 33 W. M. Zhang, X. L. Wu, J. S. Hu, Y. G. Guo, L. J. Wan, *Adv. Funct. Mater.*, 2008, **18**, 3941.
- 34 R. Wang, C. Xu, M. Du, J. Sun, L. Gao, P. Zhang and C. Lin, *Small*, 2014, DOI: 10.1002/sml.201303371.
- 35 L. Zhang, H. B. Wu, X. W. Lou, *Adv. Energy Mater.*, 2014, **4**, 1300958.
- 36 Y. Yu, C. H. Chen, J. L. Shui, S. Xie, *Angew. Chem. Int. Ed.*, 2005, **44**, 7085.
- 37 R. Wang, C. Xu, J. Sun, Y. Liu, L. Gao and C. Lin, *Nanoscale*, 2013, **5**, 6960-6967.
- 38 G. Y. Huang, S. M. Xu, J. L. Wang, L. Y. Li, and X. J. Wang, *L.Y Acta Chimica Sinica*, 2013, **71**, 1589.
- 39 H. Liu, G. X. Wang, J. Liu, S. Z. Qiao and H. J. Ahn, *J. Mater. Chem.*, 2011, **21**, 3046.
- 40 B. Wang, J. L. Cheng, Y. P. Wu, D. Wang and D. N. He, *Electrochem. Commun.*, 2012, **23**, 5.
- 41 P. Poizot, S. Laruelle, S. Grugeon, L. Dupont and J. M. Tarascon, *J. Electrochem. Soc.*, 2002, **149**, A1212.
- 42 J. Gao, M. A. Lowe and H. D. Abruña, *Chem. Mater.*, 2011, **23**, 3223.
- 43 X. P. Fang, X. L. X. W. Guo, Y. Mao, Y. S. Hu, J. Z. Wang, Z. X. Wang, F. Wu, H. K. Liu and L. Q. Chen, *Electrochem. Commun.*, 2010, **12**, 1520.
- 44 F. M. Courtel, H. Duncan, Y. Abu-Lebdeh and I. J. Davidson, *J. Mater. Chem.*, 2011, **21**, 10206.
- 45 Y. Y. Yang, Y. J. Zhao, L. F. Xiao and L. Z. Zhang, *Electrochem. Commun.*, 2008, **10**, 1117.
- 46 K. F. Zhong, X. Xia, B. Zhang, H. Li, Z. X. Wang and L. Q. Chen, *J. Power Sources*, 2010, **195**, 3300.
- 47 X. D. Liu, C. Z. Chen, Y. Y. Zhao and B. Jia, *J. Nanomater.*, 2013, 736375.
- 48 G. L. Xu, Y. F. Xu, H. Sun, F. Fu, X. M. Zheng, L. Huang, J. T. Li, S. H. Yang and S. G. Sun, *Chem. Commun.*, 2012, **48**, 8502.
- 49 X. W. Li, D. Li, L. Qiao, X. H. Wang, X. L. Sun, P. Wang and D. Y. He, *J. Mater. Chem.*, 2012, **22**, 9189.
- 50 T. Kokubu, Y. Oaki, E. Hosono, H. S. Zhou and H. Imai, *Adv. Funct. Mater.* 2011, **21**, 3673.
- 51 D. Larcher, S. Beattie, M. Morcrette, K. Edstroem, J. C. Jumas and J. M. Tarascon, *J. Mater. Chem.*, 2007, **17**, 3759.
- 52 Y. F. Deng, Q. M. Zhang, Z. C. Shi, L. J. Han, F. Peng and G. H. Chen, *Electrochim. Acta*, 2012, **76**, 495.
- 53 K. F. Zhong, B. Zhang, S. H. Luo, W. Wen, H. Li and X. J. Huang, *J. Power Sources*, 2011, **196**, 6802.
- 54 Z. H. Cui, X. X. Guo and H. Li, *J. Power Sources*, 2013, **244**, 731.
- 55 J. C. Guo, Q. Liu, C. S. Wang and M. R. Zachariah, *Adv. Funct. Mater.*, 2012, **22**, 803.
- 56 C. J. Chae, J. H. Kim, J. M. Kim, Y. K. Sun and J. K. Lee, *J. Mater. Chem.*, 2012, **22**, 17870.
- 57 W. Luo, X. L. Hu, Y. M. Sun and Y. H. Huang, *ACS Appl. Mater. Interfaces*, 2013, **5**, 1997.
- 58 Y. Xia, Z. Xiao, X. Dou, H. Huang, X. H. Lu, R. J. Yan, Y. P. Gan, W. J. Zhu, J. P. Tu, W. K. Zhang and X. Y. Tao, *ACS Nano*, 2013, **7**, 7083.

- 59 X. F. Sun, Y. L. Xu, P. Ding, M. R. Jia and G. Ceder, *J. Power Sources*, 2013, **224**, 690.
- 60 C. T. Hsieh, C. Y. Lin and J. Y. Lin, *Electrochim. Acta*, 2011, **56**, 8861.
- 61 D. F. Qiu, L. Y. Ma, M. B. Zheng, Z. X. Lin, B. Zhao, Z. Wen, Z. B. Hu, L. Pu and Y. Shi, *Mater. Lett.*, 2012, **84**, 9.
- 62 K. J. Zhang, P. X. Han, L. Gu, L. X. Zhang, Z. H. Liu, Q. S. Kong, C. J. Zhang, S. M. Dong, Z. Y. Zhang, J. H. Yao, H. X. Xu, G. L. Cui, and L. Q. Chen, *ACS Appl. Mater. Interfaces*, 2012, **4**, 658.
- 63 Y. J. Mai, D. Zhang, Y. Q. Qiao, C. D. Gu, X. L. Wang and J. P. Tu, *J. Power Sources*, 2012, **216**, 201.
- 64 Y. M. Sun, X. L. Hu, W. Luo, F. F. Xia and Y. H. Huang, *Adv. Funct. Mater.* 2013, **23**, 2436.
- 65 Y. L. Ding, C. Y. Wu, H. M. Yu, J. Xie, G. S. Cao, T. J. Zhu, X. B. Zhao and Y. W. Zeng, *Electrochim. Acta*, 2011, **56**, 5844.
- 66 B. Sun, Z. X. Chen, H. S. Kim, H. Ahn and G. X. Wang, *J. Power Sources*, 2011, **196**, 3346.
- 67 X. W. Li, S. L. Xiong, J. F. Li, X. Liang, J. Z. Wang, J. Bai and Y. T. Qian, *Chem. Eur. J.* 2013, **19**, 11310.
- 68 X. N. Li, Y. C. Zhu, X. Zhang, J. W. Liang and Y. T. Qian, *RSC Adv.*, 2013, **3**, 10001.
- 69 L. W. Su, Y. R. Zhong, J. P. Wei and Z. Zhou, *RSC Adv.*, 2013, **3**, 9035.
- 70 Y. M. Sun, X. L. Hu, W. Luo and Y. H. Huang, *J. Mater. Chem.*, 2012, **22**, 19190.
- 71 Si. R. Li, Y. Sun, S. Y. Ge, Y. Qiao, Y. M. Chen, I. Lieberwirth, Y. Yu and C. H. Chen, *Chem. Eng. J.* 2012, **192**, 226.
- 72 X. Zhang, Z. Xing, L. Wang, Y. Zhu, Q. Li, J. Liang, Y. Yu, T. Huang, K. Tang, Y. Qian and X. Shen, *J. Mater. Chem.*, 2012, **22**, 17864.
- 73 C. J. Chae, H. Y. Park, D. W. Kim, J. S. Kim, E. S. Oh and J. K. Lee, *J. Power Sources*, 2013, **244**, 214.
- 74 G. L. Xu, Y. F. Xu, J. C. Fang, F. Fu, H. Sun, L. Huang, S. H. Yang and S. G. Sun, *ACS Appl. Mater. Interfaces*, 2013, **5**, 6316.
- 75 M. M. Thackeray, W. I. F. David, P. G. Bruce and J. B. Goodenough, *Mater. Res. Bull.*, 1983, **18**, 46.
- 76 D. Pasero, N. Reeves and A. R. West, *J. Power Sources* 2005, **141**, 156.
- 77 Q. Fan and M. S. Whittingham, *Mater. Res. Soc. Symp. Proc.*, 2007, **972**, 0972-AA07-03-BB08-03.
- 78 Q. Fan and M. S. Whittingham, *Electrochim. State Lett.* 2007, **10**, A48.
- 79 P. Li, C. Y. Nan, Z. Wei, J. Lu, Q. Peng and Y. D. Li, *Chem. Mater.*, 2010, **22**, 4232.
- 80 X. P. Shen, Z. Y. Ji, H. J. Miao, J. Yang and K. M. Chen, *J. Alloys Compd.*, 2011, **509**, 5672.
- 81 W. Xiao, J. S. Chen and X. W. Lou, *CrystEngComm*, 2011, **13**, 5685.
- 82 D. P. Dubal and R. Holze, *RSC Advances*, 2012, **2**, 12096.
- 83 Z. C. Bai, B. Sun, N. Fan, Z. C. Ju, M. H. Li, L. Q. Xu, and Y. T. Qian, *Chem. Eur. J.* 2012, **18**, 15049.
- 84 Z. C. Bai, N. Fan, Z. C. Ju, C. L. Guo, Y. T. Qian, B. Tang and S. L. Xiong, *J. Mater. Chem. A*, 2013, **1**, 10985.
- 85 J. Z. Wang, N. Du, H. Wu, H. Zhang, J. X. Yu and D. R. Yang, *J. Power Sources*, 2013, **222**, 32.
- 86 Q. Hao, J. P. Wang and C. X. Xu, *J. Mater. Chem. A*, 2014, **2**, 87.
- 87 Y. Ma, C. L. Fang, B. Ding, G. Ji and J. Y. Lee, *Adv. Mater.*, 2013, **25**, 4646.
- 88 S. M. Oh, I. Y. Kim, S. J. Kim, W. Jung and S. J. Hwang, *Mater. Lett.*, 2013, **107**, 221.
- 89 T. Li, Y. Y. Wang, R. Tang, Y. X. Qi, N. Lun, Y. J. Bai and R. H. Fan, *ACS Appl. Mater. Interfaces*, 2013, **5**, 10975.
- 90 L. Ji, Z. Lin, M. Alcoutlabi and X. Zhang, *Energy Environ. Sci.*, 2011, **4**, 2682.
- 91 H. L. Wang, L. F. Cui, Y. Yang, H. S. Casalongue, J. T. Robinson, Y. Y. Liang, Y. Cui and H. J. Dai, *J. Am. Chem. Soc.*, 2010, **132**, 13978.
- 92 N. Lavoie, P. R. L. Malenfant, F. M. Courtel, Y. Abu-Lebdeh and I. J. Davidson, *J. Power Sources*, 2012, **213**, 249.
- 93 L. Li, Z. P. Guo, A. J. Du and H. K. Liu, *J. Mater. Chem.*, 2012, **22**, 3600.
- 94 S. Y. Liu, J. Xie, Y. X. Zheng, G. S. Cao, T. J. Zhu and X. B. Zhao, *Electrochim. Acta*, 2012, **66**, 271.
- 95 Z. Q. Li, N. N. Liu, X. K. Wang, C. B. Wang, Y. X. Qi and L. W. Yin, *J. Mater. Chem.*, 2012, **22**, 16640.
- 96 Z. H. Wang, L. X. Yuan, Q. G. Shao, F. Huang and Y. H. Huang, *Mater. Lett.*, 2012, **80**, 110.
- 97 C. B. Wang, L. W. Yin, D. Xiang and Y. X. Qi, *ACS Appl. Mater. Interfaces*, 2012, **4**, 1636.
- 98 I. Nam, N. D. Kim, G. P. Kim, J. Park and J. Yi, *J. Power Sources*, 2013, **244**, 56.
- 99 L. Wang, Y. H. Li, Z. D. Han, L. Chen, B. Qian, X. F. Jiang, J. Pintoc and G. Yang, *J. Mater. Chem. A*, 2013, **1**, 8385.
- 100 S. Luo, H. C. Wu, Y. Wu, K. L. Jiang, J. P. Wang and S. S. Fan, *J. Power Sources* 2014, **249**, 463.
- 101 C. Chen, H. Jian, X. X. Fu, Z. M. Ren, M. Yan, G. D. Qian and Z. Y. Wang, *RSC Adv.*, 2014, **4**, 5367.
- 102 X. J. Liu, H. Yasuda and M. Yamachi, *J. Power Sources*, 2005, **146**, 510.
- 103 P. Lavela, J. L. Tirado and C. Vidal-Abarca, *Electrochim. Acta*, 2007, **52**, 7986.
- 104 Y. Cai, S. Liu, X. M. Yin, Q. Y. Hao, M. Zhang and T. H. Wang, *Physica E*, 2010, **43**, 70.
- 105 X. P. Shen, Z. Y. Ji, H. J. Miao, J. Yang and K. M. Chen, *J. Alloys Comp.*, 2011, **509**, 5672.
- 106 Y. C. Qiu, G. L. Xu, K. Y. Yan, H. Sun, J. W. Xiao, S. H. Yang, S. G. Sun, L. M. Jin and H. Deng, *J. Mater. Chem.*, 2011, **21**, 6346.
- 107 Y. F. Deng, Z. E. Li, Z. C. Shi, H. Xu, F. Peng and G. H. Chen, *RSC Adv.*, 2012, **2**, 4645.
- 108 L. Hu, Y. K. Sun, F. P. Zhang and Q. W. Chen, *J. Alloys Comp.*, 2013, **576**, 86.
- 109 L. Chang, L. Q. Mai, X. Xu, Q. Y. An, Y. L. Zhao, D. D. Wang and X. Feng, *RSC Adv.*, 2013, **3**, 1947.
- 110 Y. H. Dai, H. Jiang, Y. J. Hu and C. Z. Li, *RSC Adv.*, 2013, **3**, 19778.
- 111 S. L. Chen, F. Liu, Q. J. Xiang, X. H. Feng and G. H. Qiu, *Electrochim. Acta*, 2013, **106**, 360.
- 112 X. Zhang, Y. T. Qian and Y. C. Zhu, *Nanoscale*, 2014, **6**, 1725.
- 113 M. W. Xu, Y. B. Niu, S. J. Bao and C. M. Li, *J. Mater. Chem. A*, 2014, **2**, 3749.
- 114 Y. H. Wang, Y. H. Wang, D. S. Jia, Z. Peng, Y. Y. Xia and G. F. Zheng, *Nano Lett.*, 2014, **14**, 1080.
- 115 J. X. Dai, S. F. Y. Li, K. S. Siow and Z. Q. Gao, *Electrochim. Acta*, 2000, **45**, 2211.

- 116 M. S. Wu, P. C. J. Chiang, J. T. Lee and J. C. Lin, *J. Phys. Chem. B*, 2005, **109**, 23279.
- 117 B. Li, G. Rong, Y. Xie, L. Huang and C. Feng, *Inorg. Chem.*, 2006, **45**, 6404.
- 118 J. Zhao, Z. Tao, J. Liang and J. Chen, *Cryst. Growth Des.*, 2008, **8**, 2799.
- 119 A. L. M. Reddy, M. M. Shaijumon, S. R. Gowda and P. M. Ajayan, *Nano Lett.*, 2009, **9**, 1002.
- 120 L. H. Li, C. Y. Nan, J. Lu, Q. Peng and Y. D. Li, *Chem. Commun.*, 2012, **48**, 6945.
- 121 J. Wang, J. Liu, Y. C. Zhou, P. Hodgson and Y. C. Li, *RSC Adv.*, 2013, **3**, 25937.
- 122 M. Kundu, C. C. A. Ng, D. Y. Petrovykh and L. F. Liu, *Chem. Commun.*, 2013, **49**, 8459.
- 123 H. Xia, M. Lai and L. Lu, *J. Mater. Chem.*, 2010, **20**, 6896.
- 124 Y. S. Yun, J. M. Kim, H. H. Park, J. Lee, Y. S. Huh and H. J. Jin, *J. Power Sources*, 2013, **244**, 747.
- 125 J. X. Lia, M. Z. Zou, Y. Zhao, Y. B. Lin, H. Lai, L. H. Guan and Z. G. Huang, *Electrochim. Acta*, 2013, **111**, 165.
- 126 Y. Wang, Z. J. Han, S. F. Yu, R. R. Song, H. H. Song, K. Ostrikov and H. Y. Yang, *Carbon*, 2013, **64**, 230.
- 127 C. X. Guo, M. Wang, T. Chen, X. W. Lou and C. M. Li, *Adv. Energy Mater.*, 2011, **1**, 736.
- 128 A. P. Yu, H. W. Park, A. Davies, D. C. Higgins, Z. W. Chen and X. C. Xiao, *J. Phys. Chem. Lett.*, 2011, **2**, 1855.
- 129 L. Li, A. R. O. Raji and J. M. Tour, *Adv. Mater.*, 2013, **25**, 6298.
- 130 Y. Zhang, H. Liu, Z. H. Zhu, K. W. Wong, R. Mi, J. Mei and W. M. Lau, *Electrochim. Acta*, 2013, **108**, 465.
- 131 Y. Y. Li, Q. W. Zhang, J. L. Zhu, X. L. Wei and P. K. Shen, *J. Mater. Chem. A*, 2014, **2**, 3163–3168.
- 132 X. Gu, L. Chen, Z. C. Ju, H. Y. Xu, J. Yang and Y. T. Qian, *Adv. Funct. Mater.*, 2013, **23**, 4049.
- 133 J. Y. Liao, D. Higgins, G. Lui, V. Chabot, X. C. Xiao and Z. W. Chen, *Nano Lett.*, 2013, **13**, 5467.
- 134 J. Fang, Y. F. Yuan, L. K. Wang, H. L. Ni, H. L. Zhu, J. L. Yang, J. S. Gui, Y. B. Chen and S. Y. Guo, *Electrochim. Acta*, 2013, **112**, 364.
- 135 M. S. Wu, P. C. J. Chiang, J. T. W. Xiao, J. S. Chen, Q. Lu and X. W. Lou, *J. Phys. Chem. C*, 2010, **114**, 12048.
- 136 L. F. Xiao, Y. Y. Yang, J. Yin, Q. Li and L. Z. Zhang, *J. Power Sources*, 2009, **194**, 1089.
- 137 Y. F. Deng, S. D. Tang, Q. M. Zhang, Z. C. Shi, L. T. Zhang, S. Z. Zhan and G. H. Chen, *J. Mater. Chem.*, 2011, **21**, 11987.
- 138 F. M. Courtel, Y. Abu-Lebdeh and I. J. Davidson, *Electrochim. Acta*, 2012, **71**, 123.
- 139 S. W. Kim, H. W. Lee, P. Muralidharan, D. H. Seo, W. S. Yoon, D. K. Kim and K. Kang, *Nano Res.*, 2011, **4**, 505.
- 140 P. F. Teh, Y. Sharma, S. S. Pramana and M. Srinivasan, *J. Mater. Chem.*, 2011, **21**, 14999.
- 141 L. Zhou, H. B. Wu, T. Zhu and X. W. Lou, *J. Mater. Chem.*, 2012, **22**, 827.
- 142 H. B. Wang, F. Y. Cheng, Z. L. Tao, J. Liang and J. Chen, *Chin. J. Inorg. Chem.*, 2011, **27**, 816.
- 143 X. F. Chen, L. Qie, L. L. Zhang, W. X. Zhang and Y. H. Huang, *J. Alloys Comp.*, 2013, 559, 5.
- 144 G. Zhang, L. Yu, H. B. Wu, H. E. Hoster and X. W. Lou, *Adv. Mater.*, 2012, **24**, 4609.
- 145 Z. C. Bai, N. Fan, C. H. Sun, Z. C. Ju, C. L. Guo, J. Yang and Y. T. Qian, *Nanoscale*, 2013, **5**, 2442.
- 146 P. F. Teh, Y. Sharma, Y. W. Ko, S. S. Pramana and M. Srinivasan, *RSC Adv.*, 2013, **3**, 2812.
- 147 J. G. Kim, S. H. Lee, Y. M. Kim and W. B. Kim, *ACS Appl. Mater. Interfaces*, 2013, **5**, 11321.
- 148 Z. M. Zheng, Y. L. Cheng, X. B. Yan, R. T. Wang and P. Zhang, *J. Mater. Chem. A*, 2014, **2**, 149.
- 149 L. J. Wang, B. Liu, S. H. Ran, L. M. Wang, L. N. Gao, F. Y. Qu, D. Chen and G. Z. Shen, *J. Mater. Chem. A*, 2013, **1**, 2139.
- 150 L. Zhou, D. Y. Zhao and X. W. Lou, *Adv. Mater.*, 2012, **24**, 745.
- 151 L. J. Wang, B. Liu, S. H. Ran, L. M. Wang, L. N. Gao, F. Y. Qu, D. Chen and G. Z. Shen, *J. Mater. Chem. A*, 2013, **1**, 2139.
- 152 M. H. Kim, Y. J. Hong and Y. C. Kang, *RSC Adv.*, 2013, **3**, 13110.
- 153 L. Yu, L. Zhang, H. B. Wu, G. Q. Zhang and X. W. Lou, *Energy Environ. Sci.*, 2013, **6**, 2664.
- 154 J. F. Li, S. L. Xiong, X. W. Li and Y. T. Qian, *Nanoscale*, 2013, **5**, 2045.
- 155 L. Hu, H. Zhong, X. R. Zheng, Y. M. Huang, P. Zhang and Q. W. Chen, *Sci. Rep.*, 2012, **2**, 986.

Table 1. Experimental values of potential for the plateaus and theoretical specific capacities associated with conversion reactions in Mn-based oxides.

Mn-based oxides	Potential (Li ⁺ /Li)	Theoretical specific capacity (mA h g ⁻¹)	Ref.
MnO	0.2	756	41
Mn ₃ O ₄	0.37	937	42
Mn ₂ O ₃	0.3	1019	43
MnO ₂	0.4	1223	43
CoMn ₂ O ₄	0.3	921	44
ZnMn ₂ O ₄	0.3	1008	45

Table 2. A summary of recent studies on MnO-based anodes for LIBs.

Materials	Preparation method	1 st discharge/charge capacity (mAh g ⁻¹)	Capacity retention	Rate performance (mAh g ⁻¹)	Ref.
MnO powder	Commercial + ball milling	~ 1266/766 at 50 mA g ⁻¹	550(10 cycles)	400 at 400mA g ⁻¹	46
MnO microspheres	Precipitation + annealing	1126/800 at 50 mA g ⁻¹	704(50cycles)	600 at 400mA g ⁻¹	53
Porous MnO nanoflakes	Hydrothermal method	781/570 at 246 mA g ⁻¹	648 (100cycles)	376 at 2460 mA g ⁻¹	49
Crystalline MnO films	Radio-frequency (RF) sputtering + annealing	550/413 at 0.05C	350(100cycles)	150 at 20C	54
Amorphous MnO _x /C	Aerosol spray pyrolysis	1083/650 at 200 mA g ⁻¹	601 (130cycles)	500 at 800 mA g ⁻¹	55
MnO _x /OMC nanocomposite	Wet-impregnation + annealing	1390/860 at 100 mA g ⁻¹	950(50cycles)	500 at 2000 mA g ⁻¹	56
Mesoporous MnO/C	Microwave-polyol process + annealing	1456/1000 at 200 mA g ⁻¹	1224(200cycles)	731 at 1500 mA g ⁻¹	57
Monodisperse MnO/C hollow microspheres	A facile biotemplating technique	1021.9/755.6 mA g ⁻¹	702.2(50cycles)	230 at 3000 mA g ⁻¹	58
(MnO/MWNTs)	Hydrothermal + annealing	1050/686 at 14.4 mA g ⁻¹	484 (200 cycles) at 144.1 mA g ⁻¹	455 at 310 mA g ⁻¹	59
MnO-attached graphene	Impregnation + annealing	685/635 at 0.2C	490 (30 cycles) at 1C	410 at 5C	60
MnO nanoparticles/graphene composite	<i>In-situ</i> carbothermal reduction	1080/700 at 100 mA g ⁻¹	782(60cycles)	402 at 1000 mA g ⁻¹	61
Nitrogen-doped MnO/graphene nanosheets	Hydrothermal method + ammonia annealing	1193/829 at 50 mA g ⁻¹	772(90cycles) at 100 mA g ⁻¹	202 at 5000 mA g ⁻¹	62
(MnO/RGOS)	Liquid phase deposition + annealing	1001/648 at 100 mA g ⁻¹	666 (50cycles)	454 at 400 mA g ⁻¹	63
MnO/graphene	Liquid phase deposition + annealing	900/891 at 200 mA g ⁻¹	2014 (150cycles)	843 at 2000 mA g ⁻¹	64
Coaxial MnO/C nanotubes	Self-templates method	1014/678 at 75.5 mA g ⁻¹	600(10cycles)	500 at 188.9 mA g ⁻¹	65
MnO/C core-shell nanorods	<i>In-situ</i> reduction method	1090/780 at 200 mA g ⁻¹	600(40cycles)		66
MnO@carbon core-shell nanowires	Solvothermal + annealing	1196/840 at 100 mA g ⁻¹	801(200cycles) at 500 mA g ⁻¹	462 at 2000 mA g ⁻¹	66
MnO@1-D carbon	Annealing of C ₄ H ₄ MnO ₆	1249/738 at 500 mA g ⁻¹	660(1000 cycles)	250 at 6A g ⁻¹	67

composites					
Porous MnO/C nanotubes	Hydrothermal method+ annealing	1129/810 at 100 mA g^{-1}	763(100cycles)	303 at 3200 mA g^{-1}	68
MnO/C nanorods	Hydrothermal method+ annealing	1408/707 at 200 mA g^{-1}	481(50cycles)	252 at 1000mA/g	69
Porous carbon-modified MnO disks	Microwave-polyol process + annealing	1387/997 at 100 mA g^{-1}	1044 (140cycles)	535 at 1000 mA g^{-1}	70
Nano-MnO/C composites	An alcoholysis process + annealing	1650/900 at 75.5mA/g	939 (30cycles)	589 at 7550 mA g^{-1}	71
MnO@C core-shell nanoplates	Hydrothermal method+ annealing	1365/770 at 200 mA g^{-1}	563(30cycles)	550 at 300 mA g^{-1}	72
MnO _x /C nanocomposite	Sol-gel method + annealing	1055/700 at 200 mA g^{-1}	500(100cycles)	320-345 at 2000 mA g^{-1}	73
Hierarchical micro/nanostructured MnO	hydrothermal method	1051/750 at 98 mA g^{-1}	783 (200cycles)	350 at 1572 mA g^{-1}	74

Table 3.A summary of recent studies on Mn₃O₄-based anodes for LIBs.

Materials	Preparation method	1 st discharge/charge capacity (mAh g ⁻¹)	Capacity retention	Rate performance (mAh g ⁻¹)	Ref.
Spongelike Nanosized Mn ₃ O ₄	Precipitation method	1327/869 at 40 mA g ⁻¹	800 (40 cycles)	500 at 10 C	43
Mn ₃ O ₄ nanorods	hydrothermal + annealing method	1050/555 at 0.1C	108(100cycles)		80
Mn ₃ O ₄ octahedral	Hydrothermal method	1009/700 at 50 mA g ⁻¹	404 (20cycles)	269 at 500 mA g ⁻¹	81
Mesoporous stacked Mn ₃ O ₄ nanosheets	Chemical bath deposition (CBD) route	824/300 at 0.1C	400(60cycles)	298 at 1.5C	82
Porous Mn _x Co _{3-x} O ₄ nanocubes	A new facile strategy	discharge 1395 at 200 mA g ⁻¹	733(30cycles)	473 at 1600 mA g ⁻¹	83
Mesoporous Mn ₃ O ₄ nanotubes	Hydrothermal +hydrogen reduction	1065/641.5 at 100 mA g ⁻¹	641(100cycles) at 500 mA g ⁻¹	525 at 1000 mA g ⁻¹	84
Order-aligned Mn ₃ O ₄ nanostructures	Electrochemically depositing method	919/622 at 936 mA g ⁻¹	882(85cycles)	500 at 40A g ⁻¹	85
Mn ₃ O ₄ octahedrons	Dealloying of MnAl alloy	918.3/536.8 at 100 mA g ⁻¹	746 (500 cycles)	240 at 1500 mA g ⁻¹	96
Fe-doped Mn _x O _y	Nanocasting technique+controlled calcination	1358/800 at 200 mA g ⁻¹	620(100cycles)	409 at 1600 mA g ⁻¹	87
Fe ₂ O ₃ -Mn ₃ O ₄ nanocomposite	electrostatically-derived selfassembly method	1050/919.8 at 90 mA g ⁻¹	230(25cycles)		88
Mn ₃ O ₄ /graphene hybrid	Two-step solution-phase reactions	1350/950 at 40 mA g ⁻¹	730 (40 cycles)	390 at 1600 mA g ⁻¹	91
Mn ₃ O ₄ /graphene composite	Ultra-sonication + annealing	1375/750 at 75 mA g ⁻¹	720(100cycles)		92
Mn ₃ O ₄ -graphene nanocomposite	Microwave hydrothermal technique	1354/901 at 40 mA g ⁻¹	900 (50cycles)	400 at 1000 mA g ⁻¹	93
Mn ₃ O ₄ /Graphite nanosheet	Solvothermal route	1079/762 at 50 mA g ⁻¹	~ 600 (50cycles)	~ 250 at 600 mA g ⁻¹	94
Mn ₃ O ₄ /ordered mesoporous carbons	Precipitation + annealing method	1843/773 at 100 mA g ⁻¹	802(50cycles)		95
Mn ₃ O ₄ /(MWCNTs) nanocomposite	Solvothermal route	1380/750 at 100 mA g ⁻¹	592(50cycles)	387 at 1000 mA g ⁻¹	96
Mn ₃ O ₄ /C nanorod	Solvothermal route	1246/723 at 40 mA g ⁻¹	473(50cycles)		97
Mn ₃ O ₄ nanoparticles/graphene	An <i>in-situ</i> transformation method	1600/700 at 60 mA g ⁻¹	500(40cycles)	200 at 1500 mA g ⁻¹	98
Mn ₃ O ₄ nanocrystals/(RGO)	Ultra-sonication-assisted method	1630/1050 at 40 mA g ⁻¹	900(20cycles)	200 at 1600 mA g ⁻¹	99

Mn ₃ O ₄ /SACNT	Thermal decomposition	≈1900/1108.4 at 1C	390(100cycles)	342 at 10C	100
Mesoporous Mn ₃ O ₄ nanosheet/graph ene	Precipitation	1553/973 at 400 mA ⁻¹	910(230cycles)	360 at 8A ⁻¹	101

Table 4 A summary of recent investigations on Mn₂O₃-based anodes for LIBs.

Materials	Pereparation method	1 st discharge/charge capacity (mAh g ⁻¹)	Capacity retention	Rate performance (mAh g ⁻¹)	Ref.
Mn ₂ O ₃ nanorods	Hydrothermal +	1509/689 at 100 mA g ⁻¹	374 (30 cycles)		104
Mn ₂ O ₃ nanofibers	annealing	1694/795 at 100 mA g ⁻¹	404 (30 cycles)		
Mn ₂ O ₃ nanowires		1611/707 at 100 mA g ⁻¹	384 (30 cycles)		
Mn ₂ O ₃ nanorods	Hydrothermal + annealing	998/349 at 100 mA g ⁻¹	~50 (100 cycles)		105
Straw-sheaf-shaped Mn ₂ O ₃	Solvothermal + annealing	1179/680 at 200 mA g ⁻¹ (0.01-2.5 V)	400 (150 cycles) at 400 mA g ⁻¹	270 at 800 mA g ⁻¹	106
Oval-shaped Mn ₂ O ₃		1159/~650 at 200 mA g ⁻¹ (0.01-2.5 V)	320 (150 cycles) at 400 mA g ⁻¹		
Porous Mn ₂ O ₃ microsphere	Solvothermal + annealing	1310/882 at 100 mA g ⁻¹	796 (50 cycles) at 100 mA g ⁻¹	470 at 2400 mA g ⁻¹	107
Porous Mn ₂ O ₃ microspheres	Solvothermal + annealing	2134/1400 at 50 mA g ⁻¹	748 (45 cycles)	423 at 1600 mA g ⁻¹	108
Mesoporous Mn ₂ O ₃ microspheres	Hydrothermal + annealing	668/~630 at 200 mA g ⁻¹	524 (200 cycles)	~ 150 at 50 mA g ⁻¹	109
Hollow Mn ₂ O ₃ nanocones	Hydrothermal + annealing	1875/909 at 50 mA g ⁻¹	280 (200cycles) at 200 mA g ⁻¹	380 at 400 mA g ⁻¹	110
Porors Mn ₂ O ₃ nanosheets	Solvothermal + annealing	1518/987 at 300 mA g ⁻¹	521 (100cycles)	500 at 500 mA g ⁻¹	111
Cubic Mn ₂ O ₃ spindle Mn ₂ O ₃	Hydrothermal + annealing	1680/780 at 100 mA g ⁻¹	~300 (55 cycles)	240 at 600 mA g ⁻¹	113
Fusiform Mn ₂ O ₃		1530/620 at 400 mA g ⁻¹	~200 (50 cycles)		
Fusiform Mn ₂ O ₃		1402/400 at 100 mA g ⁻¹	155 (40 cycles)		
Cu-doped hollow Mn ₂ O ₃ spheres	Hydrothermal + annealing	1998/1190 at 100 mA g ⁻¹	642 (100 cycles)	308 at 815 mA g ⁻¹	89

Table 5.A summary of recent studies on MnO₂-based anodes for LIBs.

Materials	Preparation method	1 st discharge/charge capacity (mAh g ⁻¹)	Capacity retention	Rate performance (mAh g ⁻¹)	Ref.
Phase-pure β -MnO ₂ nanorods	Hydrothermal + annealing	1728/488 at 0.1 mA cm ⁻²			43
Interconnected MnO ₂ nanowires	Hydrothermal + annealing	1650/800 at 85 mA g ⁻¹	~580(100 cycles)		116
Hollow α -MnO ₂ urchin	low-temperature (60 °C) mild reduction route	746/650 at 270 mA g ⁻¹	481 (40 cycles)		117
Nanoporous γ -MnO ₂ hollow microspheres	Hydrothermal + annealing	1289/1071 at 100mA g ⁻¹	657 (20 cycles)		118
Nanoporous γ -MnO ₂ nanocubes		1992/1042 at 100 mA g ⁻¹	602 (20 cycles)		
Coaxial MnO ₂ /Carbon Nanotube	Templates + infiltration + annealing	2500/880 at 50 mA g ⁻¹	500 (16 cycles)		119
α -MnO ₂ nanotubes	Exfoliation and scrolling approach	~1200/1000 at 200 mA g ⁻¹	512 (300 cycles) at 800 mA g ⁻¹		120
Hierarchical hollowmicrospheres constructed with MnO ₂ nanotubes	A bubble template-based self-scrolling method	983/830 at 300 mA g ⁻¹	700 (30 cycles)		121
Mesoporous MnO ₂ nanosheet	Electrodeposition + annealing	1643/1225 at 50 mA g ⁻¹	1690 (100 cycles) at 100 mA g ⁻¹	900 at 1000 mA g ⁻¹	122
Nanoflaky MnO ₂ /carbon nanotube	Hydrothermal method	1402/816 at 200 mA g ⁻¹	620 (50 cycles)	320 at 4000 mA g ⁻¹	123
Mesoporous γ -MnO ₂ particles/ carbon nanotube	Ultrasound irradiation	1278/741 at 50 mA g ⁻¹	934 (150 cycles)	~380 at 1000 mA g ⁻¹	124
Coaxial MWNTs@MnO ₂ @PPy	Immersing + <i>in-situ</i> polymerization	1250/730 at 100 mA g ⁻¹	820 (120 cycles)	530 at 1000 mA g ⁻¹	125
MnO ₂ nanosheets/Core-leaf onion-like carbon	Hydrothermal method	1278/854 at 50 mA g ⁻¹	541 (100 cycles)	102 at 2000 mA g ⁻¹	126
MnO ₂ /Conjugated polymer/Graphene	<i>In-situ</i> polymerization + Immersing	1835/1050 at 50 mA g ⁻¹	948 (15 cycles)	698 at 400 mA g ⁻¹	127
MnO ₂ Nanotube/Graphene	Ultra-filtration technique	1250/686 at 100 mA g ⁻¹	495 (40 cycles)	208 at 1600 mA g ⁻¹	128
Graphene-Wrapped MnO ₂ -Graphene Nanoribbons	Hydrothermal + electrostatic interaction	880/600 at 100 mA g ⁻¹	612 (250 cycles) at 400 mA g ⁻¹	580 at 1000 mA g ⁻¹	129

α -MnO ₂ /grapheme 3D network	Hydrothermal approach	1875/1150 at 60 mA g ⁻¹	998 (30 cycles)	590 at 12 A g ⁻¹	130
Porous MnO ₂ /3D graphene nanocomposites	A redox process + annealing	1554/917 at 100 mA g ⁻¹	836 (200 cycles)	358 at 1600 mA g ⁻¹	131
Porous α -Fe ₂ O ₃ branches on β -MnO ₂ nanorods	Hydrothermal + annealing	1480/1147 at 100 mA g ⁻¹	1028 (200 cycles) at 1000 mA g ⁻¹	881 at 4000 mA g ⁻¹	132
TiO ₂ -C/MnO ₂ core-double-shell nanowire	<i>In-situ</i> chemical redox	865/500 at 33.5 mA g ⁻¹	218 (150 cycles) at 3350 mA g ⁻¹	230 at 3350 mA g ⁻¹	133
ZnO/MnO ₂ sea urchin-like sleeve array	Electro-deposition	2023/878 at 200 mA g ⁻¹	1259 (100 cycles)	150 at 5000 mA g ⁻¹	134
Polythiophene (PTh)-Coated Ultrathin MnO ₂ Nanosheets	A redox process + <i>in-situ</i> polymerization	700 at 500 mA g ⁻¹	500 (100 cycles)		135

Table 6 A summary of recent studies on ZnMn₂O₄-based anodes for LIBs.

Materials	Preparation method	1 st discharge/charge capacity (mAh g ⁻¹)	Capacity retention	Rate performance (mAh g ⁻¹)	Ref.
Nanocrystalline ZnMn ₂ O ₄	Polymer pyrolysis route	1302/766 at 100 mA g ⁻¹	569 (50 cycles)		45
Flower-like ZnMn ₂ O ₄	Solvothermal method	1350/763 at 100 mA g ⁻¹	626 (50 cycles)		136
Nanocrystalline ZnMn ₂ O ₄	Coprecipitation method	1145/800 at 100 mA g ⁻¹	690 (70cycles)	365 at 1000 mA g ⁻¹	44
Nanocrystalline ZnMn ₂ O ₄	A single-source precursor route	1088/680 at 100 mA g ⁻¹	650 (200 cycles)	405 at 600 mA g ⁻¹	137
Nanocrystalline ZnMn ₂ O ₄	Hydrothermal method	1200/680 at 100 mA g ⁻¹	430 (50cycles)	75 at 2000 mA g ⁻¹	138
ZnMn ₂ O ₄ nanowires	solid-state reaction	1400/891 at 60 mA g ⁻¹	650 (40cycles)	350 at 1000 mA g ⁻¹	139
ZnMn ₂ O ₄ Nanoplates	An "escape-by-crafty-scheme" method	1277/730 at 100 mA g ⁻¹	502 (30 cycles)	324 at 1800 mA g ⁻¹	140
ZnMn ₂ O ₄ hollow microspheres	Coprecipitation + annealing method	1325/772 at 400 mA g ⁻¹	607 (100 cycles)	361 at 1600 mA g ⁻¹	141
ZnMn ₂ O ₄ hollow microspheres	solvothermal method	1335/750 at 100 mA g ⁻¹	433 (50 cycles)	245 at 400 mA g ⁻¹	142
ZnMn ₂ O ₄ hollow microspheres	Coprecipitation + annealing method	1260/830 at 100 mA g ⁻¹	599 (50 cycles)	450 at 1000 mA g ⁻¹	143
Ball-in-ball ZnMn ₂ O ₄ hollow microspheres	solvothermal + annealing method	945/6622 at 400 mA g ⁻¹	790 (120 cycles)	396 at 1200 mA g ⁻¹	144
Loaf-like ZnMn ₂ O ₄	Hydrothermal + annealing	1357/839 at 100 mA g ⁻¹	517 (100cycles) at 500 mA g ⁻¹	457 at 1000 mA g ⁻¹	145
ZnMn ₂ O ₄ nanorods	Electrospinning	1257/680 at 60 mA g ⁻¹	318 (50 cycles)		146
ZnMn ₂ O ₄ nanofibers		1469/716 at 60 mA g ⁻¹	705 (50 cycles)		
ZnMn ₂ O ₄ nanowires		1526/891 at 60 mA g ⁻¹	530 (50 cycles)		
ZnMn ₂ O ₄ mesoscale tubular arrays	A reactive template route + annealing	1198/784 at 100 mA g ⁻¹	784 (100 cycles)	364 at 1600 mA g ⁻¹	147
rGO-ZnMn ₂ O ₄ composite	A bottom-up wrapping route	1412/960 at 100 mA g ⁻¹	707 (100 cycles)	450 at 2000 mA g ⁻¹	148